

# INTERSEISMIC AND LONG-TERM DEFORMATION OF SOUTHEASTERN SICILY DRIVEN BY THE IONIAN SLAB ROLL-BACK

Amélie Viger<sup>1\*</sup>, Stéphane Dominguez<sup>1\*</sup>, Stéphane Mazzotti<sup>1</sup>,  
Michel Peyret<sup>1</sup>, Maxime Henriquet<sup>2</sup>, Giovanni Barreca<sup>3\*</sup>,  
Carmelo Monaco<sup>3</sup>, Adrien Damon<sup>1</sup>

April 22, 2024

- 1 1. Montpellier Université - CNRS, Géosciences Montpellier, France
  - 2 2. Aix-Marseille Université, CEREGE, Aix-en-Provence, France
  - 3 3. Università di Catania, Dipartimento di Scienze Biologiche, Geologiche e Ambientali, Sezione  
4 di Science della Terra, Italy
- 5 \* e-mail, amelie.viger.geo@gmail.com, stephane.dominguez@umontpellier.fr, giobarre@unict.it

## 6 Key Points

- 7 • Recent satellite geodetic data shed new light on the origin of the active deformations  
8 affecting Southeastern Sicily.
- 9 • Several deformation processes, including crustal flexure and faulting, are investi-  
10 gated to determine the most reliable mechanical explanation.
- 11 • Seismic cycle, surface, and crustal deformations of Southeastern Sicily are mainly  
12 driven by the southward migration of the Ionian slab roll-back.

## 13 Abstract:

14 New satellite geodetic data challenge our knowledge of the deformation mech-  
15 anisms driving the active deformations affecting Southeastern Sicily. The PS-InSAR  
16 measurements evidence a generalized subsidence and an eastward tilting of the Hyblean  
17 Plateau combined with a local relative uplift along its eastern coast. To find a me-  
18 chanical explanation for the present-day strain field, we investigate short and large-scale  
19 surface-to-crustal deformation processes. Geological and geophysical data suggest that  
20 the southward migration of the Calabrian subduction could be the causative geodynamic

21 process. We evaluate this hypothesis using flexural modeling and show that the com-  
22 bined downward pull force, induced by the Ionian slab roll-back, and the overloading of  
23 the Calabrian accretionary prism, is strong enough to flex the adjacent Hyblean continen-  
24 tal domain, explaining the measured large-scale subsidence and eastward bending of the  
25 Hyblean Plateau. To explain the short-scale relative uplift evidenced along the eastern  
26 coast, we perform elastic modeling on identified or inferred onshore and offshore normal  
27 faults. We also investigate the potential effects of other deformation processes including  
28 upwelling mantle flow, volcanic deflation, and hydrologic loading. Our results enable us  
29 to propose an original seismic cycle model for Southeastern Sicily, linking the current  
30 interseismic strain field with available long-term deformation data. This model is mainly  
31 driven by the southward migration of the Ionian slab roll-back which induces a downward  
32 force capable of flexuring the Hyblean crust.

33

34 **Keywords:** Southeastern Sicily, surface deformation, PS-InSAR, slab roll-back, slab pull,  
35 crustal/lithospheric flexure, extrado faulting, seismic cycle, numerical modeling

36

## 37 1 Introduction

38 Geodetic measurements, instrumental seismicity, onshore/offshore geology, and  
39 geophysics, all indicate that Southeastern Sicily is actively deforming (e.g., Azzaro and  
40 Barbano, 2000; Mastrolembo et al., 2014; Meschis et al., 2020; Anzidei et al., 2021). This  
41 region also suffered the most powerful and devastating earthquake, the 1693  $M_w \sim 7.4$   
42 Val-di-Noto earthquake, reported in the Italian seismicity catalog. This earthquake is  
43 thought to have occurred offshore the eastern margin of the Hyblean Plateau, triggering  
44 a widespread tsunami (e.g., Azzaro and Barbano, 2000; Gutscher et al., 2006; Scicchitano  
45 et al., 2022). The current geologic and tectonic framework is in line with the Cenozoic  
46 geodynamic evolution of the Central Mediterranean (Figure 1), but also appears to be  
47 influenced by the Mesozoic pre-structuration of this region (e.g., Carminati and Doglioni,  
48 2005; Frizon De Lamotte et al., 2011; Henriquet et al., 2020; Van Hinsbergen et al., 2020).  
49 In the Late Cretaceous, the Africa/Eurasia plates convergence initiated the subduction  
50 of the Alpine Tethys under the Apulia-Adria and Iberia plates, giving rise to the Alpine

51 orogeny (e.g., Handy et al., 2010, 2015; Van Hinsbergen et al., 2020; Jolivet, 2023). Dur-  
52 ing the early Cenozoic, the subduction experienced polarity reversal (e.g., Handy et al.,  
53 2010; Almeida et al., 2022) followed by, since at least the Oligocene, long-lasting slab  
54 roll-back, causing the drifting of continental micro-blocks, detached from the Iberian  
55 margin and the opening of back-arc basins throughout the Mediterranean realm (e.g.,  
56 Gueguen et al., 1998; Faccenna et al., 2001; Rosenbaum et al., 2002; Carminati et al.,  
57 2012; Van Hinsbergen et al., 2020). During the Mio-Pliocene (10-5 Myr), the collision  
58 between the southeastward migrating Calabrian-Peloritan Arc, and associated Calabrian  
59 Accretionary Prism (CAP), with the Northern African passive margin led to the forma-  
60 tion of the Sicilian fold-and-thrust belt (e.g., Gueguen et al., 1998; Henriquet et al., 2020).  
61 During the Plio-Pleistocene (5-2 Myr), the Calabrian Arc and the retreating Ionian slab  
62 continued strongly interacting with the crustal structure of the African margin, partic-  
63 ularly with the thick Pelagian continental Platform and the Malta Escarpment (Wortel  
64 and Spakman, 2000) (Figure 1). These major tectonic domains, which originated during  
65 the Triassic period, were shaped by the fragmentation of the Pangea in the early Jurassic,  
66 leading to the opening of the Neo-Tethys Ocean (e.g., Stampfli et al., 2002). Nowadays,  
67 the Calabrian subduction zone keeps moving south but at a much slower rate, suggesting  
68 that the whole system is subjected to opposing forces and/or that its driving mechanism,  
69 slab roll-back, is losing efficiency.

70

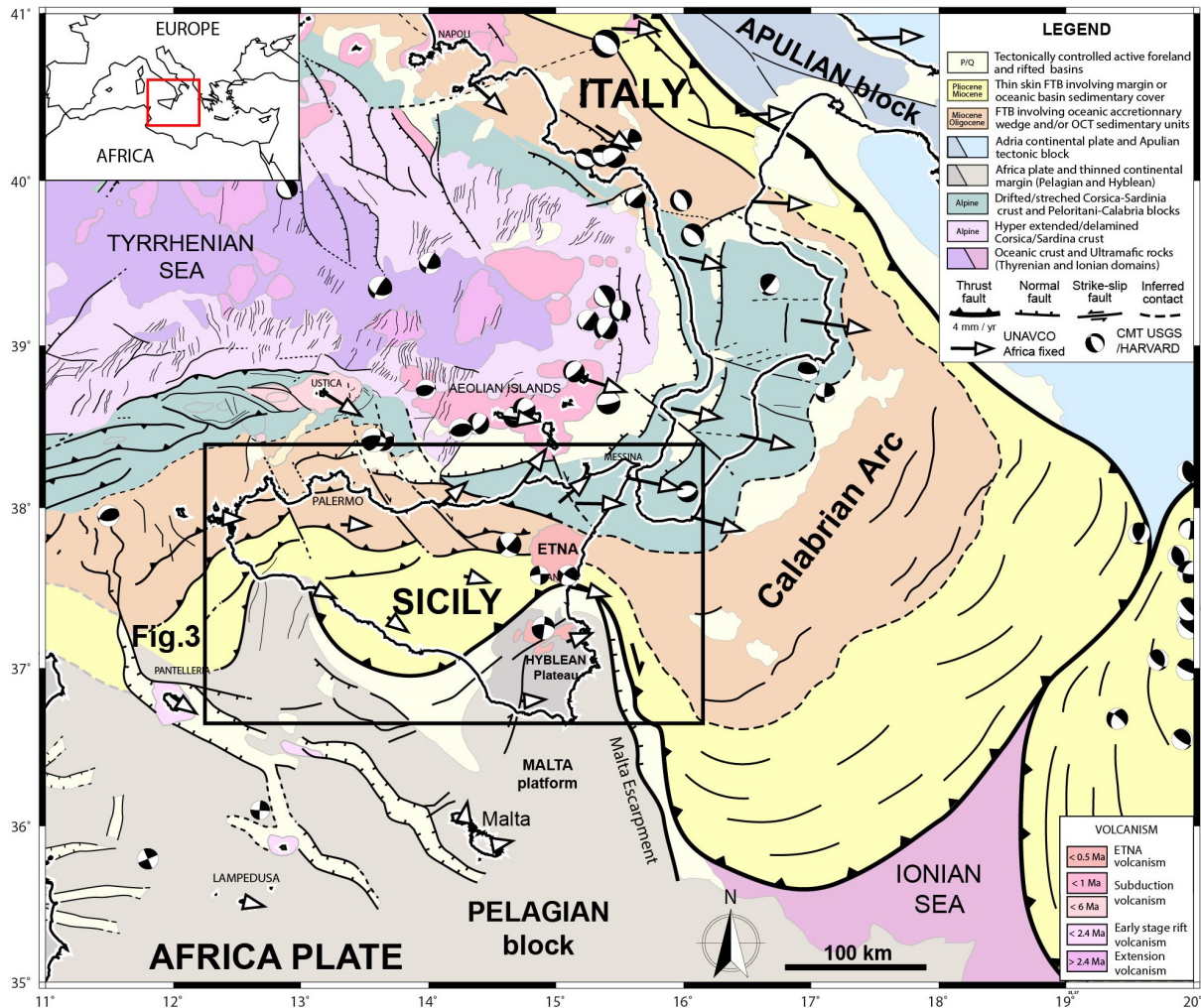


**Figure 1** : Geodynamic and tectonic map of Central Mediterranean (modified from Henriquet et al., 2020). Geological and structural data were synthesized from previous publications (e.g., Funicello et al., 1981; Bigi et al., 1991; APAT, 2005; Finetti et al., 2005; Lentini and Carbone, 2014; Prada et al., 2014). Present-day Centroid Moment Tensors ( $M_w > 4.5$ ) and GNSS data were retrieved from <https://www.globalcmt.org/CMTsearch.html> and <https://www.unavco.org/data/gps-gnss/gps-gnss.html> websites, respectively.

71 Recent PS-InSAR satellite measurements (radar interferometry), published by Hen-  
 72 riquet et al. (2022), have revealed an unexpected pattern of surface deformation across  
 73 Southeastern Sicily, particularly, an eastward increasing subsidence of the whole Hyblean  
 74 Plateau (Figure 2). This region has been partially investigated in previous studies, using  
 75 similar techniques, but only captured local surface deformation features (Canova et al.,  
 76 2012; Vollrath et al., 2017). Up to now, the origin of such a pattern of deformation re-  
 77 mains, then, unexplained. Since satellite measurements were acquired over a very short  
 78 period compared to typical seismic cycle durations (five versus several hundreds of years),  
 79 and considering the discrepancy between satellite measurements and inferred long-term  
 80 coastal uplift estimations (e.g., Bianca et al., 1999; Ferranti et al., 2006, 2010; Scicch-  
 81 itano et al., 2008; Meschis et al., 2020) (Figure 2a), we hypothesize that the satellite data



82 are representative of the interseismic period. We further infer that the PS-InSAR data  
83 mainly document elastic loading mechanisms and reversible deformations. To explain  
84 the geodetic observations, we investigate the surface deformation signature of crustal and  
85 lithospheric deformation processes, including the impact of the southward migration of  
86 the Calabrian subduction system on the structural evolution of the eastern Hyblean mar-  
87 gin as well as elastic loading and aseismic creep on coastal and offshore normal faults. We  
88 also test the potential surface expression of other processes, such as volcanic deflation,  
89 hydrologic loading, and upwelling mantle flow.

## 90 **2 Present-day deformation of SE Sicily**

91 The kinematics and active tectonics in SE Sicily are still a matter of debate, with  
92 major evolutions in the last decade (e.g., Bianca et al., 1999; Argnani et al., 2012), in par-  
93 ticular with the acquisition of high-resolution bathymetry and seismic reflection/refraction  
94 profiles in the adjacent Ionian domain (Argnani and Bonazzi, 2005; Gutscher et al., 2016;  
95 Dellong et al., 2020), and seismotectonic analysis (e.g., Gambino et al., 2021, 2022b).  
96 The main reasons include the complex polyphased geological history of this region and  
97 the relatively low present-day horizontal strain rate ( $< 5$  mm/yr), resulting from the cul-  
98 mination of the Calabrian Arc and African Margin collision, and the subsequent slowdown  
99 of the Calabrian subduction (roll-back and back-arc extension) in the last million years  
100 (Goes et al., 2004; D’Agostino et al., 2011; Zitellini et al., 2020).

### 101 **2.1 Geodesy**

102 Geodetic surface measurements in SE Sicily include GNSS (e.g., Palano et al.,  
103 2012), PS-InSAR/DInSAR (e.g., Vollrath et al., 2017), and leveling datasets (e.g.,  
104 Spampinato et al., 2013).

105

#### 106 **PS-InSAR**

107 In the present study, we use the first geodetic velocity field covering the whole  
108 Island of Sicily published by Henriquet et al. (2022) and derived from Sentinel-1 radar  
109 satellite (InSAR data) acquired during the 2015-2020 period. The PS-InSAR pseudo-3D  
110 velocity field (Up and E-W component) was obtained by merging ascending and

111 descending acquisitions, combined with a reanalysis of the GNSS time series. Due to the  
 112 acquisition geometry, the Sentinel-1 radar satellite is not sensitive to the N-S component  
 113 of horizontal surface deformation, which is, fortunately, very low in the studied region  
 114 (Henriquet et al., 2022). We therefore consider that, even if affected by minor distortions,  
 115 the Up and E-W components of the pseudo-3D velocity data can be used with confidence  
 116 (Supplementary Figures S2 to S5). The vertical (Up) component of this dataset reveals  
 117 that the central and eastern parts of the Hyblean Plateau experience subsiding rates  
 118 increasing eastward from 1 to nearly 3 mm/yr relative to the western coast (Figure 2 and  
 119 Supplementary Figure S1). It should be noted that PS-InSAR data also show a slowly  
 120 decreasing E-W component to the east of the Hyblean Plateau, with velocities evolving  
 121 from 3 to 2 mm/yr (fig.10, Henriquet et al., 2022).

122

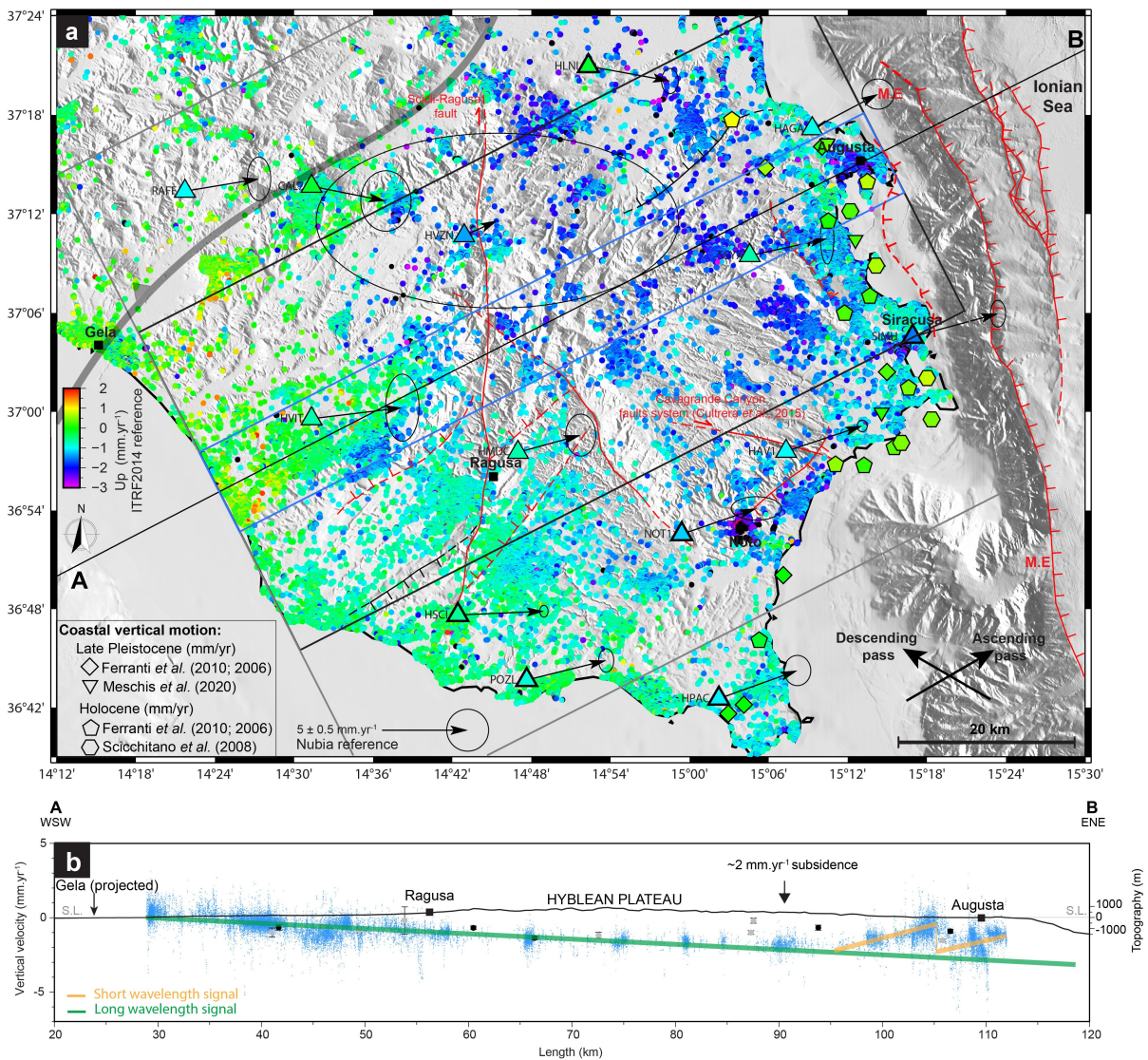


**Figure 2** : Geodetic data across the Hyblean Plateau region (see location in Figure 3). a) Permanent-Scatterer (PS-InSAR 2015-2020) pseudo-3D Up velocities in map view from Henriquet et al. (2022). GNSS 3D surface velocities are derived from a reanalysis of the Nevada Geodetic Laboratory (NGL) data (Horizontal components reference: fixed Nubia; Up components reference: ITRF2014). Major faults of the Hyblean Plateau (H.P) and Malta Escarpment (M.E) including the offshore normal faults identified by Bianca et al. (1999); Argnani and Bonazzi (2005) and recently analyzed by Gambino et al. (2021) (red: active fault; red dashed: inferred active fault; black: inferred aseismic slip from Spampinato et al. (2013)). b) SW-NE trending velocity profile showing surface velocity (Up) derived from PS-InSAR and GNSS stations vertical velocities. We observed a long wavelength signal (in green) and a short wavelength signal at the eastern part of the H.P (in orange) along the AB profile, and a similar surface deformation is observed to the South of the AB profile (Supplementary Figure S1). PS-InSAR data are stacked across a 5 km width on both sides of the AB profile (in blue). GNSS data are stacked using 20 km (in black) and 40 km (in gray) widths on both sides of the AB profile. Topographic and bathymetric profiles are presented without vertical exaggeration (V.E.x1).

123 One should note that the zero reference of the PS-InSAR vertical velocity field is  
 124 not precisely known. The vertical component of the pseudo-3D PS-InSAR velocity field  
 125 and GNSS data have a  $\pm 0.5$  mm/yr uncertainty in the ITRF2014 (Altamimi et al., 2016),  
 126 which implies that the observed subsidence over the Hyblean Plateau could be a little bit  
 127 higher or slower. In the last case, slow uplift rates could be present in the Gela region. The  
 128 vertical velocity trend is obtained by projecting and stacking the PS-InSAR data across  
 129 a 5 km wide band along an N30°E AB profile (Figure 2b). Along this profile, oriented  
 130 perpendicular to the main regional faults, the subsidence velocity reaches, on average,  $\sim 1$   
 131 mm/yr between Gela and Ragusa and increases progressively to  $\sim 2.5$  mm/yr between  
 132 Ragusa and Augusta. All along the eastern coast, a significantly slower subsidence (or a  
 133 relative uplift) is observed. From Augusta to Siracusa, and in the southernmost part of the  
 134 Hyblean Plateau (HP), the subsidence rate decreases to about 1 mm/yr compared to the  
 135 maximum subsidence rate in the central Hyblean Plateau (Figure 2). In the Gela region,  
 136 PS-InSAR vertical velocities indicate a possible slow uplift rate of  $\sim 0.5$  mm/yr (Figure  
 137 2). To the South of the AB profile, a similar surface deformation pattern is observed;  
 138 an eastward increase in subsidence rates evolving towards a similar relative uplift in the  
 139 coastal (Siracusa) region (Supplementary Figure S1).

140 Along the AB velocity profile, neither the Scicli-Ragusa inferred active fault (Voll-  
 141 rath et al., 2017), nor the other major faults of the Hyblean Plateau can be evidenced in  
 142 the E-W and vertical components of the PS-InSAR data (Henriquet et al., 2022) (Figure  
 143 2a), indicating that these faults are locked or are creeping at a slip rate lower than the  
 144 PS-InSAR resolution ( $\pm 0.5$  mm/yr). Locally, fast ( $\gg 3$  mm/yr) subsiding zones, most

145 probably related to human activities such as water pumping (Canova et al., 2012), can  
146 be identified near the main cities of Augusta, Siracusa, and Noto (Figure 2a).

147 Surface deformation signals extending over a hundred or more kilometers are  
148 most probably related to crustal or lithospheric scale processes (e.g., Stephenson et al.,  
149 2022), whereas those extending over tens of kilometers are likely associated with  
150 much shallower and localized mechanical processes such as seismic cycle deformation,  
151 volcanic bulging/collapse, hillslope instabilities (landslides), or human activities (water  
152 pumping, mining) (e.g., Vilaro et al., 2009). We therefore hypothesize that the  
153 PS-InSAR vertical velocity field consists of two superimposed signals: (1) a long  
154 wavelength ( $> 100$  km) subsidence, and gradual eastward tilt of the Hyblean Plateau  
155 (green line in Figure 2b), compatible with the decreasing PS-InSAR E-W velocities,  
156 and (2) a short wavelength signal, extending along the Eastern coast and characterized  
157 by sharp variations of the vertical velocities at kilometric scale (orange lines in Figure 2b).

158

## 159 GNSS

160 The Global Navigation Satellite System (GNSS) data used to calibrate the pseudo-  
161 3D PS-InSAR velocity field (Henriquet et al., 2022) were based on the analysis of time  
162 series, retrieved from the Nevada Geodetic Laboratory (Blewitt et al., 2018). We refine  
163 this analysis by correcting for annual and semiannual seasonal signals, instantaneous  
164 offsets, and gaps, using the time series inversion software developed by Masson et al.  
165 (2019). Across the Hyblean Plateau, GNSS velocities show horizontal velocities of  $\sim 2$   
166 mm/yr oriented homogeneously toward the ENE, in the Nubia reference frame (Figure  
167 2). The vertical component of most of the GNSS stations shows an overall subsidence  
168 of the HP ( $-0.8$  mm/yr on average) in the ITRF2014 reference frame (Altamimi et al.,  
169 2016). This tendency is well illustrated by the high-quality NOT1 GNSS station located  
170 near the city of Noto, which has recorded the longest time series (23 years, 2000-2023),  
171 or by the SSYX and HMDC stations (Supplementary Figures S2 and S3). Overall, the  
172 GNSS vertical velocities are consistent with the median of the PS-InSAR vertical velocities  
173 calculated over a  $3 \times 3$  km<sup>2</sup> region centered on each GNSS station (Supplementary Figures  
174 S2 to S5).

175 To estimate the regional horizontal strain rate tensor, we processed the GNSS  
176 dataset using the inversion model of Mazzotti et al. (2005). The Hyblean Plateau is

177 characterized by an extension rate oriented  $N55^{\circ}E \pm 1^{\circ}$  (close to the AB profile direction)  
178 and a shortening rate oriented  $N145^{\circ}E \pm 1^{\circ}$  (Supplementary Figure S6), consistent with  
179 the focal mechanisms inversion (Figure 3).

## 180 **2.2 Seismology**

181 The instrumental seismicity map of SE Sicily, derived from INGV and Rovida et al.  
182 (2022) datasets (Figure 3), shows minor to moderate events ( $M < 5$ ) with deep crustal  
183 hypocenters (15-30 km). Over the Hyblean Plateau, earthquake hypocenters tend to  
184 roughly align along the inferred active, N-S trending, Scicli-Ragusa strike-slip fault (e.g.,  
185 Vollrath et al., 2017) and near the Cavagrande Canyon faults system (Cultrera et al., 2015)  
186 (Figure 3). Most of these faults are probably inherited from the Plio-Quaternary tectono-  
187 magmatic phase of deformation (Henriquet et al., 2019) and were partly re-activated in  
188 response to the ongoing Africa-Nubia/Eurasia plates convergence (e.g., Mattia et al., 2012;  
189 Cultrera et al., 2015). In this framework, the identification of the seismogenic source that  
190 triggered the 1693 event remains debated (e.g., Argnani and Bonazzi, 2005; Bianca et al.,  
191 1999). The isoseists of the  $M_w \sim 7.4$  Noto earthquake appear largely open toward the  
192 Malta Escarpment and Ionian Sea domains, suggesting the seismogenic fault is located  
193 offshore (Figure 3). East of the Hyblean Plateau, earthquakes essentially distribute along  
194 the Malta Escarpment where a normal fault system, potentially responsible for the 1693  
195 earthquake, has been identified (e.g., Bianca et al., 1999; Argnani and Bonazzi, 2005;  
196 Gambino et al., 2021, 2022b), (Figure 3).

197 The focal mechanisms over the Hyblean Plateau have dominant strike-slip charac-  
198 teristics, contrasting with the extensional deformation characterizing the NE corner of  
199 Sicily (Figure 3).

200



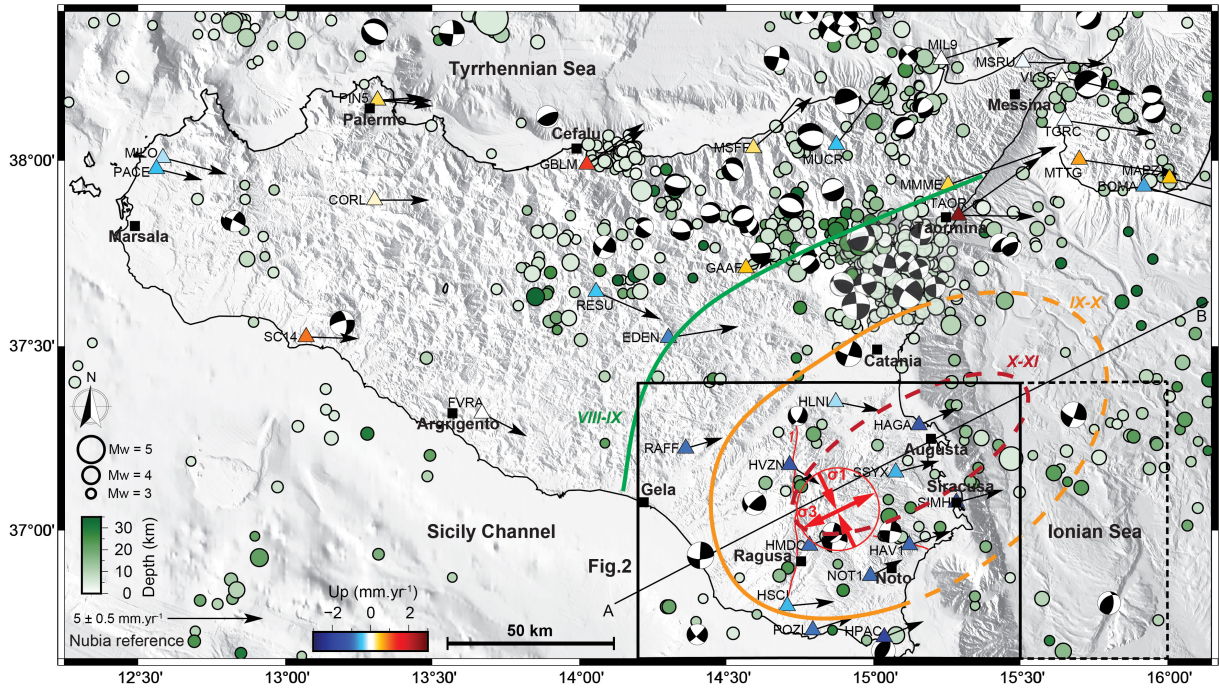


**Figure 3** : Instrumental seismicity of Sicily at crustal scale (0-30 km depth) showing earthquake hypocentral locations and focal mechanism solutions of  $M > 3$  events from 1985 to 2022 Istituto Nazionale di Geofisica e Vulcanologia (INGV) (2005); Scognamiglio et al. (2006). 3D surface velocity derived from GNSS time series published in Henriquet et al. (2022) (Horizontal components reference: fixed Nubia; Up components reference: ITRF2014). Macroseismic intensity data of the 1693 Val-di-Noto Earthquake ( $M \sim 7.4$ ) from INGV CPTI15 database (Rovida et al., 2022): red dashed line = X-XI intensity, orange dashed line = IX-X intensity, green dashed line = VIII-IX intensity). Focal mechanisms stress inversion (red arrows) for the Hyblean Plateau region (black frame) and Ionian Sea (black dashed frame) using Michael's method (Vavryčuk, 2014; Levandowski et al., 2018). The AB profile shows the location of the PS-InSAR profile and synthetic structural cross-section presented in Figures 2 and 4.

201 To estimate the present-day regional stress field across SE Sicily, we analyzed  
 202 the available focal mechanisms using the Vavryčuk's numerical model (Vavryčuk, 2014;  
 203 Levandowski et al., 2018), based on Michael's method (Michael, 1984). Results show that  
 204 the regional stress across SE Sicily (Figure 3) is homogeneous (Supplementary Figures S7  
 205 and S8). The maximum compressive stress ( $\sigma_1$ ) is horizontal and oriented  $N154^\circ E \pm 7^\circ$ ,  
 206 compatible with the  $N160^\circ E$  Africa-Eurasia plates convergence (e.g., Mattia et al., 2012;  
 207 Kreemer et al., 2014). The minimum stress ( $\sigma_3$ ) is oriented  $N64^\circ E \pm 7^\circ$ , compatible with  
 208 the extension rate derived from GNSS data inversion (Figure 3).

209 If this regional stress field is compatible with the PS-InSAR surface deforma-  
 210 tion data (E-W bending generating extensional stress), it does not explain the observed  
 211 eastward-increasing subsidence rate across the HP.

## 212 **2.3 Synthetic structural profile**

213 To constrain the deep structure and rheology of the studied area, we synthesize  
214 the available geological and geophysical data into a 200 km long simplified crustal-scale  
215 structural cross-section following the N30°E AB profile. This section incorporates part  
216 of the Hyblean Platform, the Malta Escarpment, the western Ionian domain, and cut,  
217 almost perpendicularly, the offshore normal faults along the Malta Escarpment and the  
218 Alfeo/Ionian strike-slip fault systems, extending eastward (Figures 2, 3 and 4). The  
219 eastern part of the synthetic structural profile is mainly based on seismic refraction profiles  
220 from Dellong et al. (2018, 2020), particularly the DY-P3 profile running sub-parallel to  
221 the AB profile and located 20 km further North, as well as seismic reflection profiles from  
222 Argnani et al. (2012); Gutscher et al. (2016); Tugend et al. (2019); Gambino et al. (2021,  
223 2022b) (Figure 4c). The structure of the western section is constrained by onshore and  
224 offshore geology, well log stratigraphy, geophysics, seismic reflection profiles, and geological  
225 cross-sections from the ViDEPI project, Lentini and Carbone (2014), Lipparini et al.  
226 (2023), Scarfi et al. (2018), Henriquet et al. (2019) and Finetti et al. (2005).

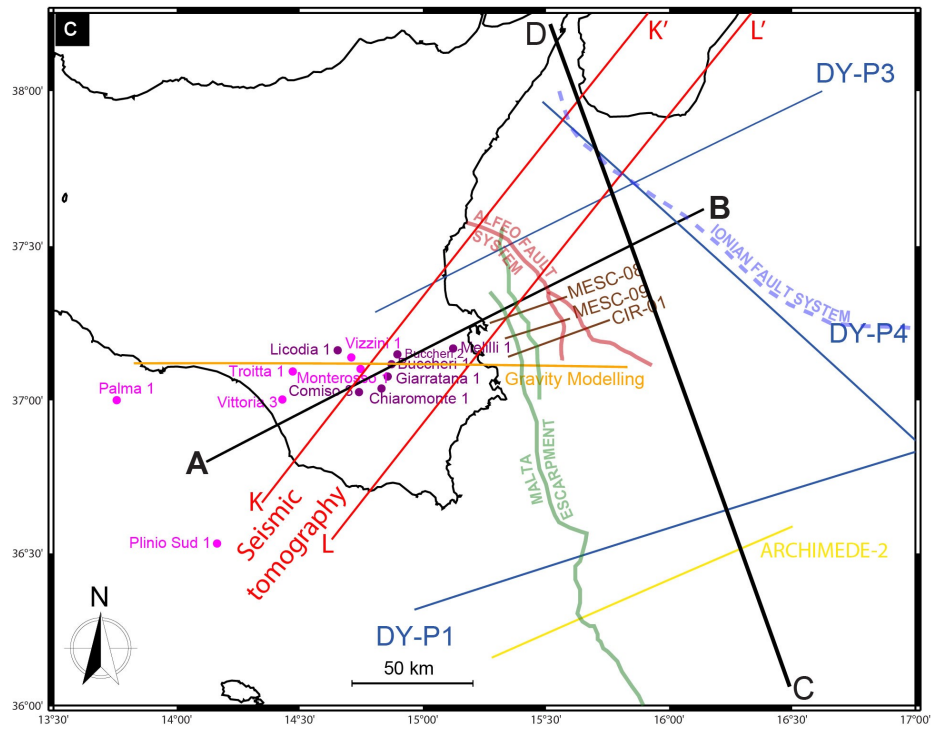
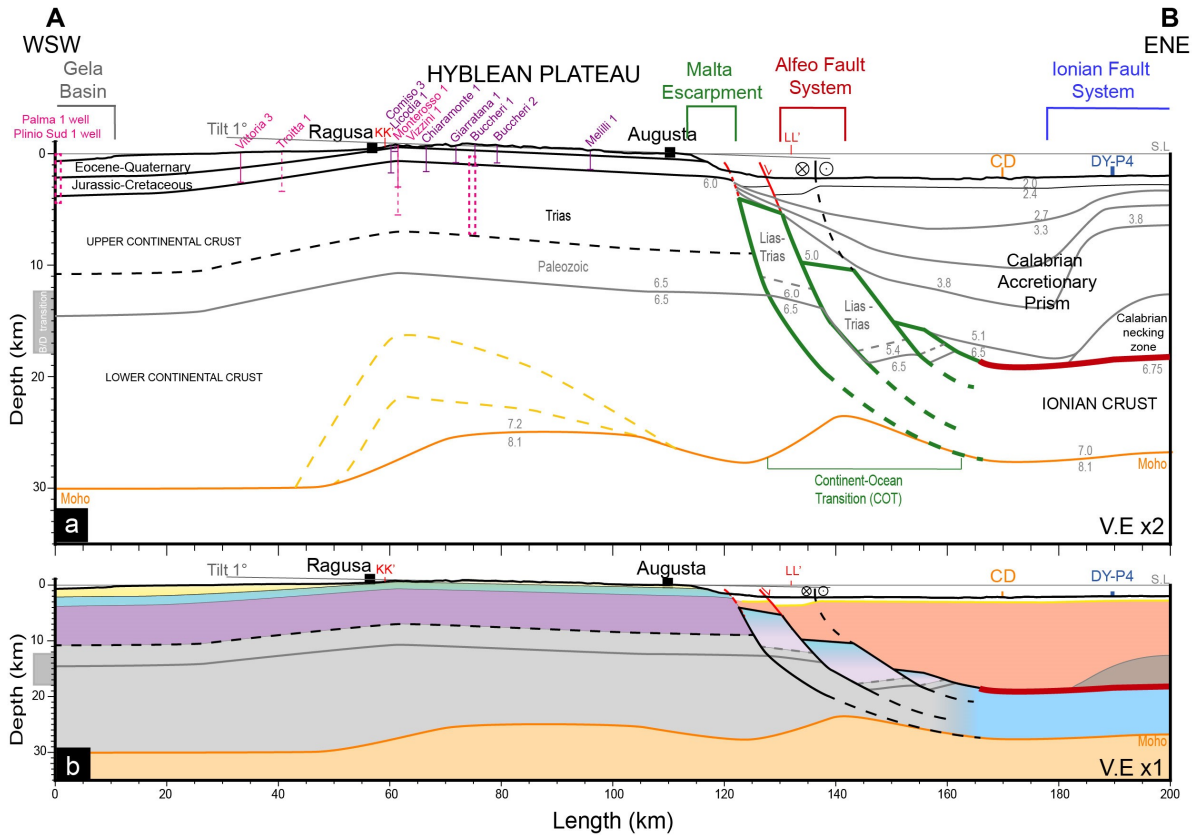




**Figure 4** : *Simplified crustal cross-section along the N30°E AB profile (see Figures 4c and 2 for location). a) Two times vertically exaggerated synthetic structural profile along with seismic velocity data showing the structure and rheology of the Hyblean Plateau and eastern oceanic domain determined from onshore and offshore geology, wells stratigraphy, geophysics, seismic reflection, and refraction profiles (see Supplementary Figure S9 for references). Note the 1° tilt of the Hyblean Plateau topography toward the East. The red line corresponds to the inferred position of the main subduction décollement, and the green lines, refer to our interpretation of tilted blocks from the Malta Escarpment (M.E). b) The synthetic structural profile shows the potential geological layers and structural deduced by, essentially, wells data for onshore domain and seismic refraction for offshore domain profiles, respectively, without vertical exaggeration (V.E.x1). c) Locations, in map view, of the AB profile, wells data, tomography profile, refraction, and reflection seismic profiles.*

227 In the Hyblean domain, geophysical data (e.g., SgROI et al., 2012; Milano et al., 2020)  
228 indicate that the crust has an average thickness of ~30-35 km, with a notable difference  
229 in the Hyblean Plateau region, marked by a huge positive Bouguer anomaly. Based on  
230 gravity data modeling, Henriquet et al. (2019) showed that this gravity anomaly can be  
231 explained by a 100 km-large high-density lower crustal body, compatible with a local  
232 Moho uplift to a depth of about 20-25 km. This last interpretation seems also supported  
233 by recent tomographic data (Scarfi et al., 2018). We constrain the geometries of the  
234 Quaternary to Mesozoic sedimentary units of the Hyblean Platform and Gela basin are  
235 constrain using the Monterosso 1, Plinio Sud 1, Troitta 1, Vittoria 3, Vizzini 1 wells from  
236 ViDEPI project (in pink, Figure 4c and Supplementary Figure S9), the Chiaramonte 1 and  
237 Mellili 1 wells from Lentini and Carbone (2014), and Buccheri 1-2, Comiso 3, Giarratana  
238 1 and Licodia 1 wells from Lipparini et al. (2023) (in purple, Figure 4c and Supplementary  
239 Figure S9). We also used the top of the Upper Triassic (Gela formation) isobaths published  
240 by Lipparini et al. (2023).

241 In the DY-P3 seismic refraction profile (Dellong et al., 2018), the 6.0 and 6.5 km/s  
242 velocity contours delimit two main steps deepening eastward at the junction between  
243 the Hyblean continental and Ionian oceanic domains (Figures 4a and 4b). Considering  
244 their locations along the Malta Escarpment that outlines the Continent-Ocean Transition  
245 (COT), we interpret these velocity variations as deepening of the sediment/basement  
246 boundary, potentially related to tilted blocks of thinned continental crust formed during  
247 the Permo-Triassic/Early Jurassic rifting phase (see section 1) (e.g., Scandone et al., 1981;  
248 Minelli and Faccenna, 2010; Dellong et al., 2018; Tugend et al., 2019). Our interpretation  
249 of tilted blocks at the continent-ocean transition is consistent with similar considerations  
250 analyzing seismic reflection/refraction profiles (e.g., Afilhado et al., 2015; Sapin et al.,

251 2021; Klingelhofer et al., 2022).

252 As documented in Argnani and Bonazzi (2005), Gutscher et al. (2016), and Gambino  
253 et al. (2021, 2022b), the seismic reflection profiles (MESC-O6, MESC-11, CIR-01, MESC-  
254 08, and MESC-09) show several normal faults bounding and crossing the Turbiditic Valley,  
255 extending along the base of the Malta Escarpment (Gutscher et al., 2016). The Turbiditic  
256 Valley fault system is constituted by three parallel normal faults,  $\sim 60$  km long, producing  
257 a marked morphological offset of the Ionian seafloor from the latitudes of Catania to  
258 Siracusa (Figures 4a and 4b). These faults dip  $35\text{-}50^\circ$  to the East and most probably  
259 merge at depth into a single major fault plane (Argnani and Bonazzi 2005; Argnani 2021;  
260 cf. MESC-08 and MESC-09 seismic reflection profiles in Gambino et al. 2021). These  
261 offshore normal faults could be linked to the recent re-activation of crustal faults at the  
262 Ocean-Continent Transition, inherited from the Early Mesozoic rifting phase (Figures 4a  
263 and 4b).

264 On the eastern side of the Hyblean domain, the Moho is constrained by DY-P3  
265 and DY-P1 refraction profiles to a depth of  $\sim 30$  km below the Malta Escarpment. To the  
266 east, in response to the bending of the Ionian slab, the Moho deepens northward from 20  
267 km (DY-P1) to 32 km (DY-P3). Based on these data and the DY-P4 refraction profile  
268 (Dellong et al., 2020), we estimate the depth of the Moho below the Ionian oceanic crust  
269 to be about 25-30 km in the eastern part of the AB synthetic profile. In this region, the  
270 domain delimited by the seismic refraction velocities of 3.8-5.1 km/s has been interpreted  
271 as corresponding to the deformed sediments of the Calabrian accretionary prism (CAP)  
272 (Dellong et al., 2018). Its thickness increases from 5 km (DY-P1) to 15 km (DY-P3), and  
273 it is evaluated to be  $\sim 15$  km along the AB profile (Figures 4a and 4b). Note that a portion  
274 of the southern termination of the Calabrian Arc (i.e., Hercynian basement) is probably  
275 present in the AB profile according to the seismic refraction DY-P4 profiles (Dellong et al.,  
276 2020) (Figures 4a and 4b). The location of the main subduction décollement along the  
277 AB profile has been estimated at a depth of  $\sim 20$  km (thick red line in Figure 4a) using  
278 the velocity of 6.75 km/s seismic refraction DY-P3 and DY-P4 profiles (Dellong et al.,  
279 2018).

### 3 Mechanical model hypotheses

To explain the long wavelength bending trend evidenced by the PS-InSAR Up component, we model the flexure of the Hyblean Plateau induced by (1) overloading of the continent-ocean transition (COT) domain in response to the SE migration of the very thick Calabrian accretionary prism (CAP), and (2) forced subsidence of the COT due to the local increase of the slab pull force imposed by the southward roll-back of the Ionian subduction. We hypothesize that these crustal/lithospheric deformation mechanisms may be strong enough to bend the adjacent Hyblean domain and induce the large-scale subsidence and tilt evidenced by the geodetic data (PS-InSAR and GNSS) (Figure 2b). In addition, we test interseismic loading models on several onshore and offshore east-dipping normal faults, such as the Augusta-Siracusa fault, the Malta Escarpment, and the active faults documented by Bianca et al. (1999); Argnani and Bonazzi (2005), Gutscher et al. (2016) and Gambino et al. (2021, 2022b), to explain the short wavelength deformation signal (relative uplift) extending along the eastern coast of the Hyblean Plateau (Figure 2b).

#### 3.1 Lithospheric flexure along a NNW-SSE profile

To better constrain key flexural parameters, such as the rigidity of the Hyblean and Ionian crust/lithospheres, the slab-pull force, and to investigate the impact of the Ionian slab roll-back, we first model the bending of the subducting Ionian slab along a NNW-SSE profile (CD profile), trending orthogonal to the AB profile (Figure 5a). We compare the Ionian slab geometries with Hayes et al. (2018) and Maesano et al. (2017) datasets with the depth of the top oceanic crust from Dellong et al. (2018) seismic refraction data (Supplementary Figure S10). In the southern part of the CD profile, the Maesano et al. (2017) dataset indicates shallower depths ( $\sim 5$  km), compared to Hayes et al. (2018) and Dellong et al. (2018, 2020) data, because the main décollement jumps away from the top of the Ionian oceanic crust to a higher level in the sedimentary cover (Supplementary Figure S10). Note that in the northern part of the CD profile, the Maesano et al. (2017) dataset indicates also shallower depth compare to Hayes et al. (2018) dataset.

Finally, we decided to use, as a structural reference, the isobaths of the top of the Ionian slab published by Hayes et al. (2018), because it correlates with the top of the

310 oceanic crust depths derived from the seismic refraction data (Dellong et al., 2018, 2020)  
311 (Figure 5a).

312 The lithosphere flexure models (as well as those in section 3.2) are calculated  
313 using the gFlex software (Wickert, 2016). We impose a no-displacement condition at the  
314 southern profile boundary and a broken plate with no bending moment and no shear at  
315 the northern boundary. The Ionian oceanic lithosphere is modeled assuming an effective  
316 elastic thickness ( $T_e$ ) ranging from 25 to 37 km (Figure 5b and Supplementary Figure S11)  
317 compatible with its Triassic to early Jurassic age (e.g., Catalano et al., 2001; Speranza  
318 et al., 2012) and consistent with other publications (e.g., Watts and Zhong, 2000; Tesauero  
319 et al., 2012; Cloetingh et al., 2015).

320 The flexure of the subducting slab depends on its mechanical properties and the  
321 loads induced by the sedimentary cover, the accretionary prism, and the slab pull force  
322 (Figure 5b). According to seismic refraction profiles DY-P1 and DY-P4 (Dellong et al.,  
323 2018, 2020), the undeformed ante-Messinian sedimentary cover overlying the Ionian crust  
324 has a thickness of about 5 km. Thus, taking into account a depth of the Ionian Sea of  
325 5-6 km, we consider that the top of the Ionian crust was lying at a uniform depth of  
326 10-11 km before the onset of the Calabrian subduction system (Figure 5b). This depth  
327 corresponds to the isostatic equilibrium for the Ionian crust. It determines the initial  
328 geometry of the flexural model from which we calculate the bending induced by the  
329 Calabrian accretionary prism (CAP) load.

330

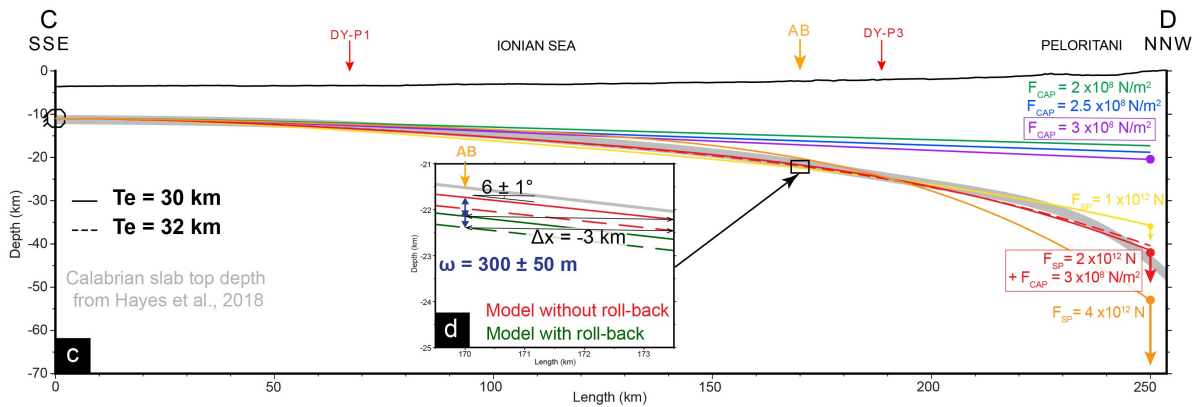
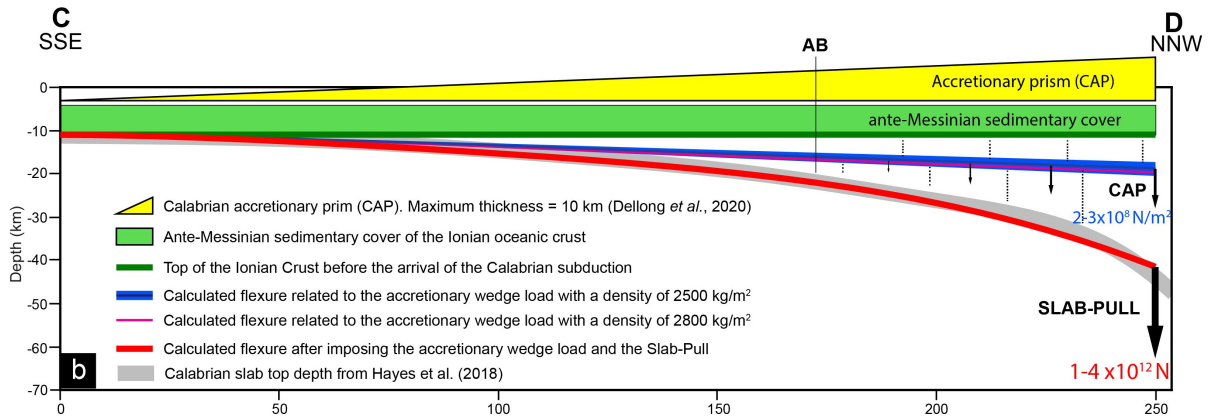
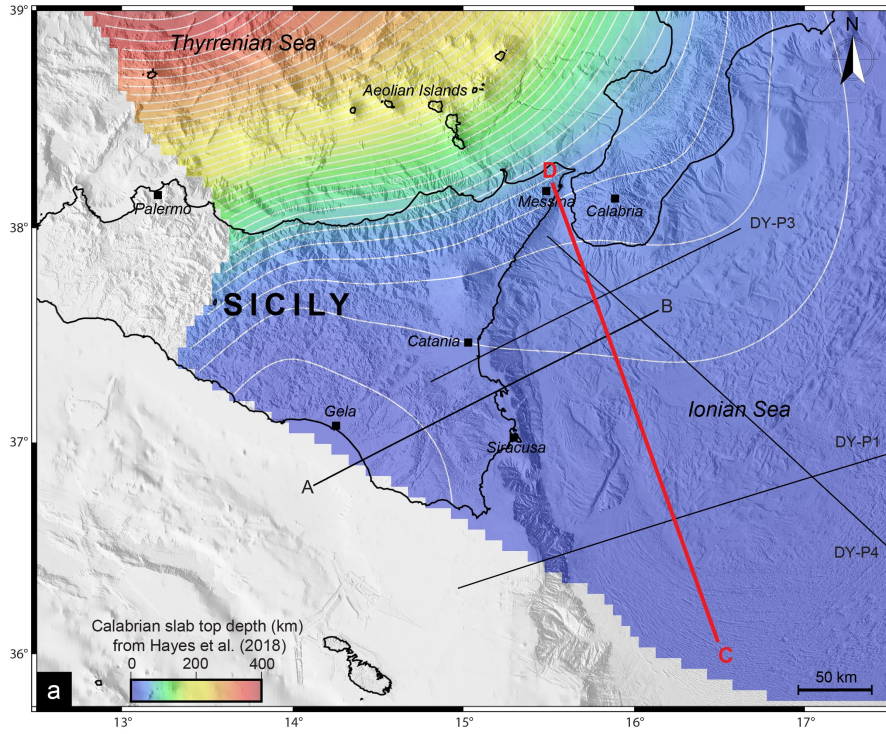


**Figure 5 :** a) Map and isobaths of the top of the Ionian slab subducting below the Calabrian Arc (Hayes et al., 2018) with seismic refraction profiles from Dellong et al. (2018, 2020), also used to constrain the top of the Ionian oceanic crust. b) NNW-SSE trending CD cross-section (in gray) showing the flat and ramp geometry of the Ionian slab (see location in Figure 5a). The Ionian oceanic lithosphere supports a 5 km thick homogeneous Paleogene sedimentary cover (in green). The CAP (in yellow) thickness increases northward up to  $\sim 15$  km (Dellong et al., 2020). The associated flexure (in blue) is calculated with density ranging from  $2500 \text{ kg/m}^2$  to  $2800 \text{ kg/m}^2$  (in dark blue and pink). The bending of the slab is controlled by the slab pull, represented as a punctual load, ranging from  $1\text{-}4 \times 10^{12}$  N (in red). c) The Paleogene cover and the CAP load are performed with a maximum CAP load of  $2 \times 10^8\text{-}3 \times 10^8 \text{ N/m}^2$ . Flexural models are performed with effective elastic thicknesses ( $T_e$ ) ranging from 25 to 37 km and slab pull forces ranging from  $1 \times 10^{12}$  to  $4 \times 10^{12}$  N (Supplementary Figure S11). Topographic, slab, and flexural model profiles are presented without vertical exaggeration (V.E.x1). d) Zoom of profiles CD and AB intersection showing the depth difference between favorite models: CAP load of  $3 \times 10^8 \text{ N/m}^2$ , slab pull of  $2 \times 10^{12}$  N, elastic thickness of 30 (continuous line) and 32 (dashed line) km, without rollback (red line) and with rollback (green line). The local subsidence associated with the 3 km/Myr slab SE retreat is estimated to be about  $300 \pm 50$  m.

331 Based on seismic refraction profiles DY-P4, DY-P1, and DY-P3 (Dellong et al., 2018,  
 332 2020), the Calabrian accretionary prism thickness increases northward from 5 to 15 km.  
 333 By removing the initial 5 km-thick Ionian sedimentary cover, the CAP load represents  
 334 an increase in sediment thickness from 0 km at the southern end of the CD profile to 10  
 335 km at the northern end. The Calabrian backstop, made of Hercynian continental crust,  
 336 is not taken into account (Figure 5b).

337 The CAP load is calculated by:

$$F_{CAP} = \rho gh \quad (1)$$

338 with a sediment density ( $\rho$ ) of  $2500\text{-}2800 \text{ kg/m}^2$  (profile 2D) using to Dellong et al. (2020),  
 339 a gravity acceleration ( $g$ ) of  $9.81 \text{ m/s}^2$ , and an increase of the CAP thicknesses ( $h$ ) from 0  
 340 to 10 km. We also calculated the CAP load using an end-member density of  $2800 \text{ kg/m}^2$   
 341 (Figure 5b), which resulted in a variation in flexure amplitude of a few percent, thus not  
 342 affecting the results of continental flexural models.

343 The CAP load ( $F_{CAP}$ ) is applied on the CD profile divided into 1-km-long segments  
 344 by imposing a northward linear gradient from 0 to  $2.45 \times 10^8 \text{ N/m}^2$  (equation 1) on the  
 345 first 250 km of the profile (Figures 5b and 5c). We perform several tests with different  
 346 maximum CAP load ( $F_{CAP}$ ) and elastic thicknesses ( $T_e$ ) ranging from  $2 \times 10^8$  to  $3 \times$   
 347  $10^8 \text{ N/m}^2$  and 25 to 37 km, respectively. Models are tested with a constant mantle density  
 348 of  $3300 \text{ kg/m}^2$  and no filling density for mantle restoration force (Figure 5c). The resulting  
 349 flexure ( $\sim 8$  km maximum), even if significant, is not sufficient to fit the Ionian slab profile

350 (gray line in Figures 5b and 5c).

351 The slab pull force is then added to the northern termination of the Ionian litho-  
352 sphere as a point load (Figure 5b). Flexural models are tested with different slab pull  
353 forces ranging from  $1 \times 10^{12}$  to  $4 \times 10^{12}$  N, consistent with other publications reviewing  
354 slab rollback mechanical properties (e.g., Lallemand et al., 2008) and the same range of  
355 elastic thicknesses from 25 to 37 km (Figure 5c and Supplementary Figure S11). The best  
356 fit to the Ionian slab top profile is obtained for elastic thicknesses ( $T_e$ ) of 30-32 km, a  
357 maximum accretionary wedge load ( $F_{CAP}$ ) of  $3 \times 10^8$  N/m<sup>2</sup>, and a slab pull force ( $F_{SP}$ ) of  
358  $2 \times 10^{12}$  N (Figure 5c and Supplementary Figure S11). It's worth noting that including  
359 the CAP load significantly reduces the amplitude of the forebulge associated with slab  
360 bending, resulting in a flat-and-ramp geometry similar to that of the Ionian slab.

### 361 **3.2 Crustal flexure along a WSW-ENE profile**

362 The impact of the Ionian subduction roll-back on the deformation of the Hyblean  
363 Plateau is evaluated along the N30°E trending AB profile (Figure 5a), considering the fol-  
364 lowing simplifications: (1) The ongoing roll-back induces incremental changes in the slab  
365 profile that can be matched with a southward translation of the slab geometry, inducing a  
366 local deepening. (2) This results in a local incremental increase of the accretionary prism  
367 thickness. (3) Due to the mechanical coupling of the Ionian slab and Hyblean lithosphere,  
368 the slab deepening exerts an incremental downward force on the COT (Figure 6).

369 The effective elastic thickness of the Hyblean lithosphere is less constrainable than  
370 that of the Ionian lithosphere but should remain within standard values for a regular  
371 undeformed continental crust with an average geotherm. We test elastic thicknesses ( $T_e$ )  
372 ranging from 25 to 40 km (Figure 6), assuming a uniform thickness, considering that the  
373 continent-ocean transition and the oceanic lithosphere have the same elastic rigidity as  
374 the Hyblean crust. Finally, we also considered that none of the fault systems offshore  
375 SE Sicily are mature enough to significantly affect the mechanical properties of the  
376 above-mentioned crustal/lithospheric blocks (e.g., Gambino et al., 2022a).

377

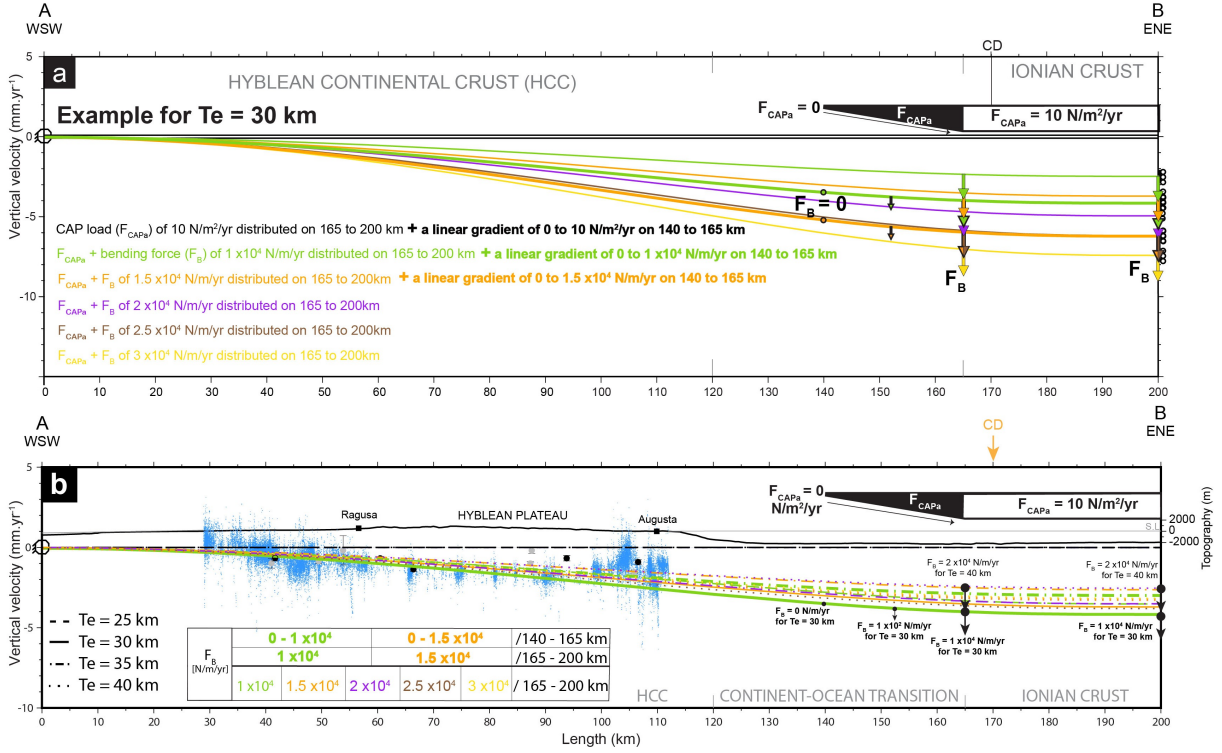


**Figure 6 :** a) Continental crustal flexure is controlled by the southward retreat of the Ionian slab. We calculated the flexure ( $gFlex$  from Wickert, 2016) induced by the only CAP load ( $F_{CAPa}$ ) of  $10 \text{ N/m}^2/\text{yr}$  distributed on the Continent-Ocean Transition (in black), and on the adjacent Ionian crust (in white). For an elastic thickness of  $30 \text{ km}$ , best models have a bending forces ( $F_B$ ) of  $1 \times 10^4 \text{ N/m/yr}$  (in green),  $1.5 \times 10^4 \text{ N/m/yr}$  (in orange),  $2 \times 10^4 \text{ N/m/yr}$  (in purple),  $2.5 \times 10^4 \text{ N/m/yr}$  (in brown), and  $3 \times 10^4 \text{ N/m/yr}$  (in yellow) distributed on the only adjacent Ionian crust or including also part of the COT (see also Supplementary Figure S12). b) Best models (Supplementary Figure S12) are compatible with a wide range of elastic thicknesses ( $25\text{-}40 \text{ km}$ ). PS-InSAR vertical velocities (in blue) and GNSS vertical velocities with their uncertainties. Topographic and bathymetric profiles are presented without vertical exaggeration ( $V.E.x1$ ).

378 We first evaluate the flexural response due solely to the local incremental increase  
 379 of the CAP load induced by its southward migration, using our previous analysis of the  
 380 bending of the Ionian slab. Based on the velocities of the GNSS stations situated in  
 381 Calabria, we estimate the southward migration to  $3 \text{ mm/yr}$ , compared to a fixed Hyblean  
 382 Plateau (Henriquet et al., 2022). At the intersection between AB and CD profiles, at  
 383 the  $170 \text{ km}$  length mark in the CD profile, the Ionian slab dips  $6 \pm 1^\circ$  toward the north  
 384 (Hayes et al., 2018) (Figure 5d). Taking into account the CAP geometry, its southward  
 385 motion, and the slab geometry, we calculate a local incremental thickening of the CAP  
 386 of  $3 \times 10^{-4} \text{ m/yr}$  (equivalent to  $300 \text{ m/Myr}$ ) and a resulting load ( $F_{CAPa}$ ) of about  $5\text{-}$   
 387  $10 \text{ N/m}^2/\text{yr}$  (Figure 5d). Applying a linear load gradient starting from zero at the base  
 388 of the Malta Escarpment ( $140 \text{ km}$  marks of the AB profile) to  $5\text{-}10 \text{ N/m}^2/\text{yr}$  at the end  
 389 of the continent-ocean transition ( $165 \text{ km}$  marks of the AB profile), then applying this  
 390 constantly load until the end of the AB profile results in a slow onshore subsidence rate of



391  $1.5 \times 10^{-4} \pm 5 \times 10^{-5}$  mm/yr maximum, 20 000 time smaller than the PS-InSAR subsidence  
 392 rate measured in the same area ( $\sim 3$  mm/yr).

393 We then investigate the effect of the southward Ionian slab roll-back and associ-  
 394 ated downward pull on the COT. We first calculate the flexural rigidity of the oceanic  
 395 lithosphere (Turcotte and Schubert, 2014):

$$D = \frac{ETe^3}{12(1 - \nu^2)} \quad (2)$$

396 with a Young modulus (E) of  $1 \times 10^{11}$  Pa, a Poisson's ratio ( $\nu$ ) of 0.25, and effective  
 397 elastic thicknesses (Te) of 30-32 km (see 3.1). We obtain a flexural rigidity (D) of the  
 398 Ionian lithosphere of  $2.4\text{-}2.9 \times 10^{23}$  Pa m<sup>3</sup>.

399

400 To simulate the Ionian slab retreat, we translate the slab profile southward, as-  
 401 suming a slab retreat velocity of  $\sim 3$  mm/yr (D'Agostino et al., 2011) (Figure 5d). At  
 402 the intersection of profiles AB and CD, this induces an incremental deepening of the Io-  
 403 nian slab of about  $3 \times 10^{-4}$  m/yr (equivalent to 300 m/Myr), which defines the equivalent  
 404 downward force at the same location along the CD flexure profile (Turcotte and Schubert,  
 405 2014):

$$F_B = \frac{\omega 2D}{x^2(L - \frac{x}{3})} \quad (3)$$

406 with an incremental deflection ( $\omega$ ) of  $3 \times 10^{-4}$  m/yr (Figure 5d) and a flexural rigidity  
 407 (D) of  $2.4\text{-}2.9 \times 10^{23}$  Pa m<sup>3</sup>. The total profile length L corresponds to the point of the  
 408 Hyblean lithosphere where the deflection ( $\omega$ ) is null,  $\sim 200$  km based on the PS-InSAR and  
 409 structural data (Figure 6). The distance x corresponds to the point where the deflection  
 410 ( $\omega$ ) is estimated (intersection with profile CD). Considering  $L = 250 \pm 50$  km and  $x =$   
 411  $150$  km, the equivalent incremental downward force is about  $1\text{-}6.5 \times 10^4$  N/m/yr.

412 This equivalent force ( $F_B$ ) is then applied on the AB profile to model, with gFlex,  
 413 the resulting flexure of the Hyblean crust/lithosphere. Flexural models are calculated  
 414 with a no-displacement boundary condition at the southwestern end of the profile (20 km  
 415 west of Gela) and a free displacement of a horizontally clamped boundary condition at  
 416 its northeastern end (80 km East of Malta Escarpment). Flexural models are run with  
 417 a fill density of  $2500$  kg/m<sup>2</sup> (2D profile) solely for the CAP load. The downward force

418 ( $F_B$ ) and CAP load ( $F_{CAPa}$ ) are applied as constant loads (on 1-km-long segments) over  
419 the 35 or 60-km long portion of the AB profile corresponding to the only adjacent Ionian  
420 crustal domain, and from the base of the Malta Escarpment to the end of the COT, as a  
421 linear load gradient evolving from zero to the maximum calculated load. We test different  
422 elastic thicknesses ( $T_e$ ) and bending force ( $F_B$ ) ranging from 25 to 40 km and  $1 \times 10^4$  to  
423  $6.5 \times 10^4$  N/m/yr, respectively (Figure 6b and Supplementary Figure S12).

424 To determine the best Hyblean crustal flexure models, we first filter the PS-InSAR  
425 vertical velocities (5 km stacked of the AB profile) using a 5 km width median filter with a  
426 step of 1 km. Comparing the resulting long-wavelength trend of the PS-InSAR data with  
427 all flexural models shows maximum misfits of about 12 mm/yr. The comparison between  
428 the GNSS data (20 km stacked of the AB profile and 5 km large median filter with a step  
429 of 1 km) shows a little bit higher maximum misfit of about 13 mm/yr due to a variable  
430 spatial density and quality of GNSS stations over the Hyblean Plateau (Supplementary  
431 Figure S12c). The best models (0.5 mm/yr RMS PS-InSAR) have a CAP load plus a  
432 bending force ranging from  $1 \times 10^4$  to  $3 \times 10^4$  N/m/yr distributed on a 35 km long portion  
433 of the AB profile, and also between  $1 \times 10^4$  to  $1.5 \times 10^4$  N/m/yr distributed on a 60 km  
434 long portion of the AB profile, with effective elastic thicknesses ranging from 25 to 40  
435 km (Figure 6b, and Supplementary Figures S12b, S12c). None of the tested continental  
436 crustal flexure models reproduce the short wavelength deformations observed in the Gela  
437 region (slow uplift of  $\sim 0.5$  mm/yr) or along the Augusta-Siracusa coastal area (relative  
438 uplift of 1-2 mm/yr).

### 439 **3.3 Interseismic loading and aseismic creep on coastal and off-** 440 **shore faults**

441 Along the coast, from Augusta to Siracusa, PS-InSAR vertical velocities vary at  
442 a kilometer-scale and appear 1-3 mm/yr slower than the general trend of subsidence  
443 affecting the Eastern Hyblean Plateau (Figures 2a and 6b). Interestingly, these short  
444 wavelength signals show triangular patterns similar to those produced by shallow faulting  
445 in an elastic domain. To investigate the sources of these surface deformations, we test  
446 several scenarios involving interseismic loading and aseismic creep on coastal and offshore  
447 faults.

448 Offshore, several active normal faults, outcropping along the base of the Malta Es-  
449 carpment, have been identified, imaged and documented in detail by Argnani and Bonazzi  
450 (2005); Gutscher et al. (2016); Gambino et al. (2021, 2022b). Close to the coastline, the  
451 offshore Augusta-Siracusa fault (Figure 7) has also been considered as a potential active  
452 fault (e.g., Bianca et al., 1999; Azzaro and Barbano, 2000). We use the Coulomb 3.4  
453 software (Toda et al., 2011) to impose different fault slip rates and geometric boundary  
454 conditions on these fault systems, assuming standard elastic properties (Poisson's ratio of  
455 0.25, Young modulus of 80 GPa).

456 The fault plane geometries tested (strike, dip) are based on published field-trip  
457 observations and measurements (Gambino et al., 2021). Fault locations are based on  
458 published geological/structural maps (Adam et al., 2000) and on the presence of sharp  
459 gradients in the PS-InSAR velocity pattern. The imposed fault slip velocities result from  
460 a trial-and-error empirical approach. The objective, essentially, is to evaluate if aseismic  
461 slip on known and unknown faults could generate sufficient surface deformation to explain  
462 the measured surface deformation pattern.

463 The model predictions are compared to the PS-InSAR short wave-length signals  
464 (Figure 7b) obtained by removing the mean of best-fitting flexural models (see section  
465 3.2) from the original geodetic dataset. Two patterns of relative uplifts of about  $2.5 \pm$   
466  $0.5$  mm/yr, gently tapering westward, can be identified near and to the SE of Augusta  
467 with a zone of relative subsidence of about  $-2 \pm 1$  mm/yr in between them (Figure 7a).  
468 We hypothesized that these surface deformations could be induced by fault slip along  
469 ENE-dipping normal fault systems (Figure 7).

470

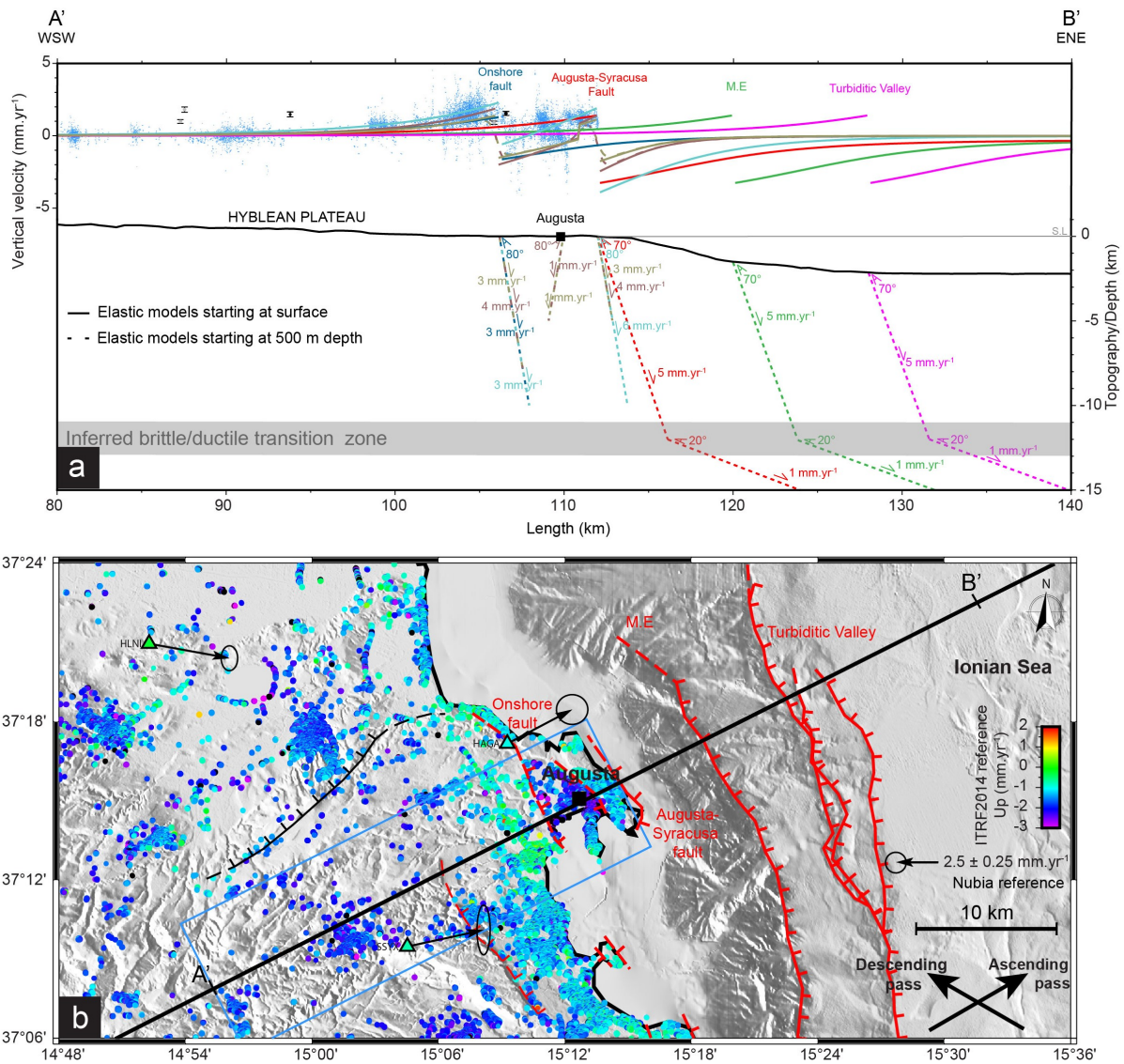


**Figure 7 :** a) Coulomb 3.4 (Toda et al., 2011) numerical models of interseismic elastic loading on offshore and coastal inferred active faults along the eastern Hyblean Platform. PS-InSAR Up velocities (in blue) are stacked across a 5 km width on both sides of the AB profile. Modeled interseismic deformations related to: the Turbiditic Valley normal fault (in magenta); the Malta Escarpment (in green); the Augusta-Siracusa coastal fault (in red); onshore inferred active faults in Augusta (in dark blue). Modeled elastic loading of the Augusta-Siracusa coastal fault plus onshore inferred active faults in Augusta are represented in light blue, light, and dark brown lines. Topography/depth is represented without vertical exaggeration ( $V.E.x1$ ). b) Map view of geodetic data in the northeastern part of the Hyblean Plateau. Major faults of the Hyblean Plateau including the Augusta-Siracusa coastal fault and the inferred onshore active fault, and Malta Escarpment (M.E) including the Turbiditic Valley faults (red: active fault; red dashed: inferred active fault; black: inferred aseismic slip).

471 The first set of models corresponds to interseismic locking of the shallow (0 to  
 472 10-15 km depth) sections of the main normal faults identified in the study area (Figure  
 473 7b) and elastic loading by deep ( $> 15$  km depth) creeping sections. Regardless of the  
 474 deep fault geometry or slip rates, all these models generate generalized long-wavelength  
 475 subsidence rates incompatible with the geodetic data (green dotted line, Supplementary  
 476 Figure S13). Thus, we dismiss interseismic loading as a potential mechanism to explain

477 the short wavelength surface deformation patterns.

478 The second set of models corresponds to shallow aseismic slip imposed on three  
479 offshore normal faults: the Augusta-Siracusa fault (Bianca et al., 1999), the Malta Es-  
480 carpment fault, and the Turbiditic Valley fault (Gutscher et al., 2016; Gambino et al.,  
481 2021, 2022b) (Figure 7a and Supplementary Figure S13). We decided to test the Malta Es-  
482 carpment fault because it lies between the Turbiditic Valley active fault and the Augusta-  
483 Siracusa fault, for which evidence of activity has been documented by as yet unpublished  
484 sparker lines acquired in the Augusta Bay (G. Barreca, C. Monaco, personal commu-  
485 nication). The modeled faults (Figure 7a) share a similar listric geometry with a first  
486 fault plane dipping  $70^\circ$ NE and extending from the surface to 12 km depth (inferred brit-  
487 tle/ductile transition zone) and a second one dipping  $20^\circ$ NE and extending from 12 to  
488 50 km depth (to limit boundary effects). We imposed slip rates of 5 mm/yr on the first  
489 fault plane, based on Meschis et al. (2020) model (Supplementary Figure S13), and 1  
490 mm/yr on the second plane to dampen the elastic deformation produced by slip on the  
491 shallow fault (Figure 7a). Aseismic slip on these various faults produces coastal uplift  
492 rates, reaching at most  $\sim 1$  mm/yr for the Augusta-Siracusa fault, consistent with the  
493 PS-InSAR measurements east of Augusta (Figure 7a). However, all the modeled offshore  
494 faults failed to reproduce the  $\sim 2$ -3 mm/yr relative uplift rates measured west of Augusta  
495 (Figures 7a and 7b).

496 The third set of models focuses on surface deformation generated by aseismic creep  
497 on  $70$ - $80^\circ$  ENE-dipping shallow coastal and onshore fault planes. We first simulate slip on  
498 the upper portion of the Augusta-Siracusa fault, but if this model succeeds in producing  
499 sufficient uplift east of Augusta, it fails to reproduce the relative uplift west of Augusta.  
500 Based on PS-InSAR data and structural evidence of regional onshore normal faulting (e.g.,  
501 Adam et al., 2000; Gambino et al., 2021), we added to the previous Augusta-Siracusa fault  
502 model an  $80^\circ$  dipping onshore normal fault outcropping at the 106 km mark of the AB  
503 profile (sharp velocity gradient in the PS-InSAR data), with a slip rate of 3 mm/yr down  
504 to 10 km depth (light blue lines in Figure 7a). The surface deformation generated by this  
505 dual creeping fault can explain the observed PS-InSAR relative uplift between the 103  
506 and 106 km profile marks and 110 and 112 km. Note that imposing aseismic slip on the  
507 onshore normal fault alone fails to reproduce the subsidence east of Augusta (dark blue  
508 line in Figure 7a).

509 The triangular patterns of sharp steps and associated lows in the PS-InSAR data  
510 could be also fitted by a three-fault model, involving shallower aseismic creep (up to 5 to  
511 8 km depth) and combining the onshore ENE-dipping fault (106 km mark), creeping at  
512 3-4 mm/yr, with an antithetic onshore WSW-dipping fault (110 km mark), creeping at  
513 1 mm/yr, and the Augusta-Siracusa coastal fault (112 km mark), creeping at 3-4 mm/yr  
514 (brown lines in Figure 7a). We test the same configuration (two onshore faults and the  
515 Augusta-Siracusa coastal fault) with a fault plane propagating to the surface up to 500  
516 m depth (Figure 7a). This model, equivalent to a blind fault, induces vertical surface  
517 deformation (between the 106 and 110 km marks) about 0.2 mm/yr slower than the  
518 model starting to creep from the surface but remains consistent with the PS-InSAR data.

519 All this ad-hoc model, illustrates that the short wavelength geodetic signal along  
520 the Eastern Hyblean Plateau coast could be explained by ongoing extension tectonics and  
521 creep on coastal normal faults.

### 522 **3.4 Alternative hypothesis**

523 To explore if other natural processes could explain part of the observed geodetic  
524 velocity patterns, we briefly investigate three alternative models:

525

#### 526 **Mantle flow upwelling**

527

528 Seismic tomography and volcanic data identify a slab window extending along  
529 most of the northern coast of Sicily, with a slab break-off recently propagating from  
530 west to east and potentially triggering toroidal and upwelling mantle flows (Trua et al.,  
531 2003; Civello and Margheriti, 2004; Faccenna et al., 2005; Scarfi et al., 2018). This  
532 process could induce long wavelength surface motions (so-called dynamic topography)  
533 over the whole Sicily. However, mantle flow numerical modeling mainly predicts  
534 areas of uplift and subsidence restricted to Mount Etna and the southern Peloritani  
535 region (Faccenna et al., 2011; Gallen et al., 2023). Thus, SE Sicily appears to be  
536 situated too far from the Ionian slab edge to be affected by upwelling mantle flow. There-  
537 fore, it is unlikely that this hypothesis explains the observed vertical surface deformations.

538

## 539 **Volcanic deflation**

540

541 The last volcanic activity documented on the Hyblean Plateau dates back 1.4  
542 Myr (Schmincke et al., 1997; Behncke, 2004), but recent magmatic activity, not recorded  
543 at the surface, cannot be ruled out. In such a case, volcanic material deflation located  
544 below the central Hyblean Plateau could induce local subsidence rates affecting a large  
545 region. We tested this hypothesis numerically with deflating spheres, 6 to 14 km in  
546 diameter, (Mogi model, Supplementary Figure S14) situated at a depth of 8 km, at the  
547 top of the Paleozoic basement and possible location of magma accumulation (Henriquet  
548 et al., 2019). Our first-order tests show that even using extreme deflations of 50-75%, the  
549 PS-InSAR subsidence rates cannot be reproduced (Supplementary Figure S14), rendering  
550 the volcanic deflation hypothesis extremely unlikely.

551

## 552 **Hydrological loading**

553

554 The geology of the Hyblean Platform is mainly composed of limestones and  
555 dolomites in a karstic environment. Long-term recharge or discharge of karst aquifers  
556 is known to induce transient elastic deformation, measurable geodesically (e.g., Grillo  
557 et al., 2011; Silverii et al., 2016; D'Agostino et al., 2018). Hydrological loading/unloading  
558 cycles can have a significant impact on vertical deformation, up to a few tens of mil-  
559 limeters on an annual cycle (White et al., 2022). The effects of hydrological variation on  
560 pluri-annual trends are more difficult to assess. Here we consider velocities over 5 years  
561 from PS-InSAR and GNSS. The regional subsidence rate of 1-3 mm/yr and associated  
562 east-side-down tilt would require an average increase of the water level by  $\sim 10$ -20 cm over  
563 5 years at the scale of the whole Southeastern Sicily reservoir. This seems incompatible  
564 with the absence of similar observable effects over Central and Western Sicily, and with  
565 the drought periods that have affected Sicily in recent decades. Hydrological loading, as  
566 a source of large-scale surface subsidence, is then unproved.

## 567 4 Discussions

### 568 4.1 Short-term and long-term model limits

569 We explain the eastward tilt and subsidence rates of the Hyblean Plateau as the  
570 flexure of the Hyblean continental crust/lithosphere induced by the southward migra-  
571 tion of the Calabrian Accretionary Prism (CAP) and retreat of the Ionian subducting  
572 slab (sections 3.1 and 3.2). This model is based on the assumption that the geodetic  
573 data (GNSS and PS-InSAR), measured over a short period (5-15 years), are represen-  
574 tative of the kinematic evolution of the studied region at the scale of a few hundred  
575 to a thousand years. In the absence of significant seismic events during the period of  
576 geodetic data acquisition, and considering that major earthquakes ( $M > 7$ ) in SE Sicily  
577 probably have a return period of more than 500 years, geodetic data are mainly recording  
578 interseismic elastic deformation and possibly, minor permanent one (fault creep, fold-  
579 ing, human-related surface deformation). Flexural modeling indicated that the increasing  
580 loading of the COT, induced by the southward propagation of the CAP, is not suffi-  
581 cient (Figure 6b). The increase in bending force, imposed by a  $\sim 3$  mm/yr southward  
582 retreat of the Ionian slab, gives interesting positive results. This process could be strong  
583 enough to pull down the Eastern termination of the Hyblean crust at velocities compat-  
584 ible with PS-InSAR measurements. However, we obtained this result considering that  
585 the Hyblean crust/lithosphere, the Continent-Ocean Transition (COT), and the Ionian  
586 crust/lithosphere have similar mechanical properties. The Alfeo-Etna fault system, in  
587 particular, was considered not mature enough offshore SE Sicily to alter significantly the  
588 mechanical properties of the above-mentioned crustal/lithospheric blocks (Gambino et al.,  
589 2022a). This assumption implies that the COT has a significantly rigid and potentially  
590 too strong rheology (Figure 8), as discussed hereafter (section 4.2).

591 We used simple 2D elastic models based on parameters determined through ana-  
592 lytical modeling of the Ionian oceanic lithosphere flexure using, as a reference, the Ionian  
593 slab geometry determined by Hayes et al. (2018), and data (depth of the top of the Io-  
594 nian crust) extracted from the refraction profiles published in Dellong et al. (2018). The  
595 use of more advanced numerical models (FEM), including 3D modeling methods, would  
596 likely improve our first-order estimates. Similarly, the lateral variations of the Hyblean  
597 continental crust thickness and elastic properties are not accurately known. We used the



598 available geophysical data (Scarfi et al., 2018; Henriquet et al., 2019), but it was not possible to constrain the Hyblean crust/lithosphere rheology with better confidence (Figure 600 8). Should such parameters become available in the future, they could be used to refine our Hyblean crust/lithosphere flexure calculations.

602 One of the other assumptions we made concerns the rate of increase in the slab bending force due to the southward propagation of the Ionian slab roll-back. The calculated increase in slab bending force east of the HP is based on the estimated rate of southward retreat of the Ionian slab defined by the mean of the GNSS NS horizontal velocities in southwest Calabria (using as a reference Malta Island). However, this estimate may be understated if the Calabrian Arc migrates southward more slowly than the Ionian slab retreat, due to lateral mechanical interactions with the Apulian and African margins.

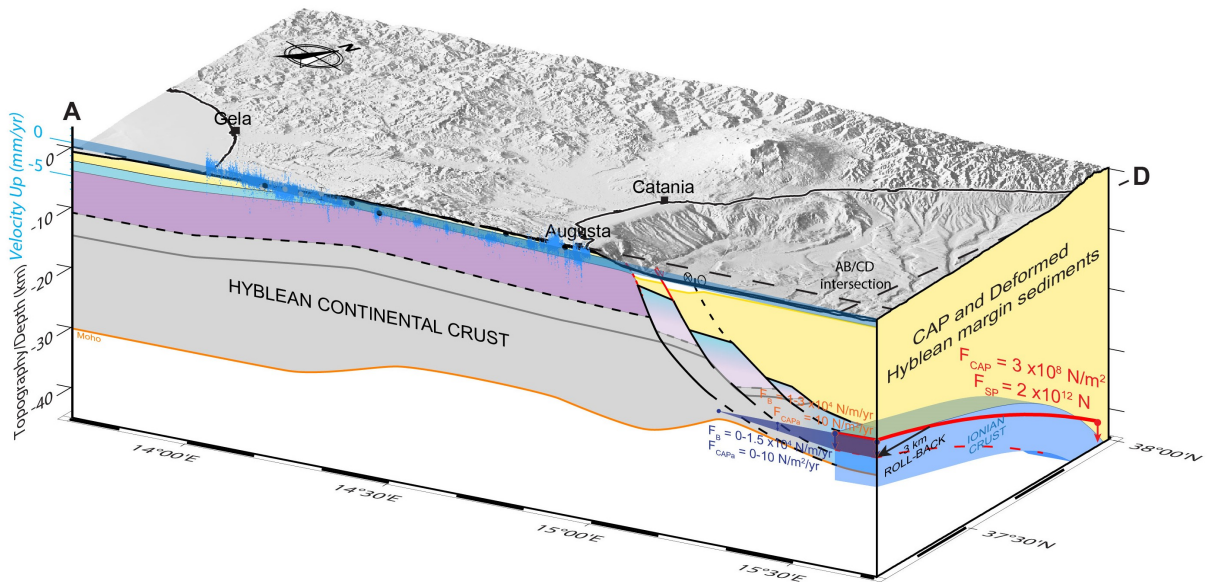


**Figure 8 :** Schematic 3D deformation model of Southeastern Sicily controlled by Ionian slab roll-back delimited by profiles AB and CD. The 3 km southward retreat of the Ionian crust flexure model (red dashed line) has a horizontal exaggeration of 6 times. The Moho of the Hyblean continental crust determined by geophysical data (Scarfi et al., 2018; Henriquet et al., 2019) is shown in orange. The Calabrian accretionary prism (CAP) and deformed Hyblean margin sediments are shown in yellow. The synthetic structural profile in AB profile have no vertical exaggeration (V.E x1).

609 The short-wavelength relative uplift signal, observed in the geodetic data along the Southeastern Sicily coast, must be driven by more shallow deformation mechanisms than those responsible for the long-wavelength eastward flexure of the HP (Figure 6b). Kilometer long surface deformations are typically related to upper crustal deformation processes (e.g., Burgmann and Thatcher, 2013), so we test interseismic loading models on the inferred and identified onshore and offshore fault systems.

615 Slip on the Malta Escarpment and Turbiditic Valley normal fault cannot explain  
616 the observed deformation of the eastern coast of the Hyblean Plateau. Only creep on the  
617 Augusta-Siracusa coastal fault and the antithetic structure (Bianca et al., 1999; Azzaro  
618 and Barbano, 2000) induce onshore vertical deformation compatible with the geodetic  
619 data near Augusta. Interseismic slip (creep) on two onshore ENE and WSW 80°-dipping  
620 faults, and the Augusta-Siracusa coastal fault fits with the PS-InSAR data in the Eastern  
621 of the AB profile. These faults could re-activate inherited Permo-Triassic to Early Jurassic  
622 NW-SE extensional structures, leading to the formation of the Augusta Graben, extending  
623 up to Siracusa (e.g., Grasso and Lentini, 1982). Even if some seismic activity affects  
624 this region (e.g., Adam et al., 2000; Azzaro and Barbano, 2000), field evidence of recent  
625 (Holocene) tectonic activity has yet to be demonstrated.

626 Our results suggest that these faults should creep up to the surface or the near-  
627 surface (blind fault) to produce sufficient interseismic surface deformation in the footwall.  
628 In that later case, their surface expressions could correspond to gentle surface folding or  
629 to fold scarp morphologies (e.g., Chen et al., 2007; Li et al., 2015) rather than localized  
630 cumulated fault scarps.

631 High precision leveling data acquired between 1970-1991 and analyzed by Spamp-  
632 inato et al. (2013), reveals a remarkable  $\sim 4$  mm/yr velocity offset between benchmarks  
633 107 and 113, both situated near the coast 5 km west of Augusta (Figure 9c). This sharp  
634 vertical velocity gradient is correlated with a marked topographic step, trending NS,  
635 and descending toward the sea. Northwest of Augusta, the leveling dataset also shows a  
636  $\sim 2$  mm/yr offset between benchmarks 119 and 120, associated with a topographic step,  
637 oriented E-W, and facing north (Figures 9b and 9c).

638

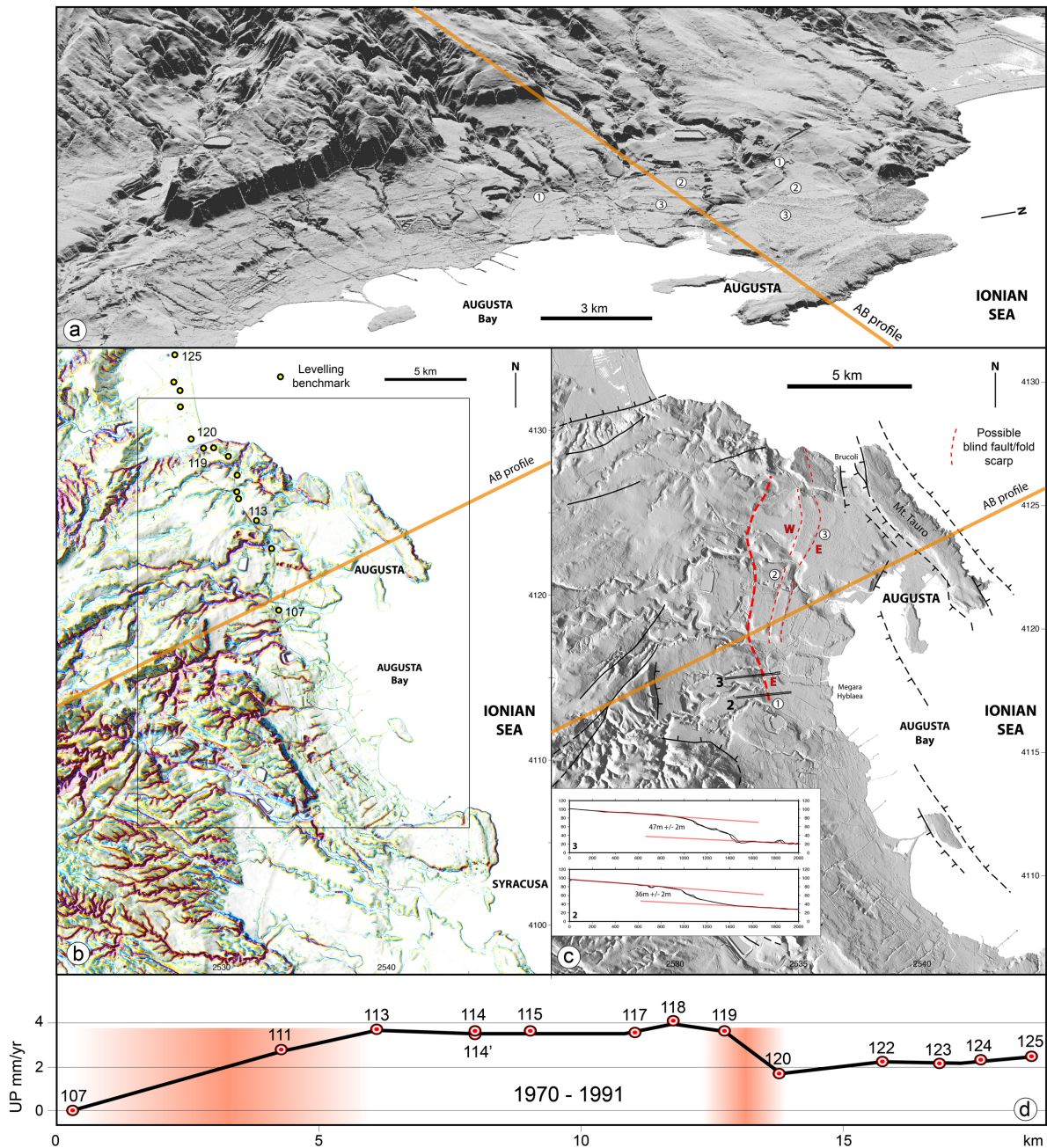


**Figure 9 :** a) 3D view of a shaded DEM of 2 m resolution from S.I.T.R. regione Siciliana (2013) showing the morphology of the NE part of the Hyblean Plateau. b) Morphological map of the Augusta-Syracusa region showing fluvial incision networks and morphological scarps. The location of leveling benchmarks appears in yellow circles. c) Simplified morpho-structural map highlighting the location of potential tectonic fault/fold scarps in red, and the know fault in thick red dashed line with cross-sections (Supplementary Figure S15). d) 1970-1991 leveling profile (Spampinato et al., 2013) showing a first velocity step ( $\sim 4$  mm/yr) between benchmark 107 and 113, and a second one ( $\sim 2$  mm/yr), between benchmark 119 and 120 (potential fault zone locations appear in the background in red).

639 A morpho-structural analysis of this region, using a 5 m resolution DEM, outlines  
 640 sharp drainage incision anomalies oriented perpendicular to the identified topographic  
 641 steps, potentially related to tectonic surface uplift (Figure 9b). The topographic step  
 642 between benchmarks 119 and 120 (Figures 9a and 9d) could correspond to the Scordia-  
 643 Lentini Graben border (e.g., Cultrera et al., 2015). The topographic anomaly between

644 benchmarks 113 and 107, extending to the north up to the Ionian Sea and to the South  
 645 toward Siracusa, was not previously identified as a tectonic feature. It could correspond to  
 646 the implemented creeping fault used to match the PS-InSAR data. Uplifted late Quater-  
 647 nary marine terraces have been evidenced in this region (Bianca et al., 1999; Monaco and  
 648 Tortorici, 2000; Meschis et al., 2020), but the authors didn't mention a tectonic origin for  
 649 the measured coastal uplift. Finally, the measured fast surface uplift (1-2 mm/yr) could  
 650 be considered as inconsistent with the low amplitude of the topographic scarp measurable  
 651 in the field (a few tens of meters). This point is discussed hereafter (section 4.2).

## 652 4.2 Combined long-term tectonics and seismic cycle model

653 The subsidence and tilt patterns observed in the geodetic data can be explained  
 654 by the combination of (1) the flexure of the Hyblean continental crust induced by the  
 655 bending force generated by the Ionian subduction roll-back (slab-pull) and the CAP  
 656 overload, explaining the long-wavelength deformation affecting the HP, and (2) the  
 657 aseismic activity of the Augusta-Siracusa fault system, potentially extending onshore an  
 658 inferred tectonic structures, explaining the short-wavelength deformation signal affecting  
 659 the Augusta/Siracusa region (Figure 10). In this section, we discuss how this short-term  
 660 (geodetic) model could be combined with long-term geological and tectonic observations.

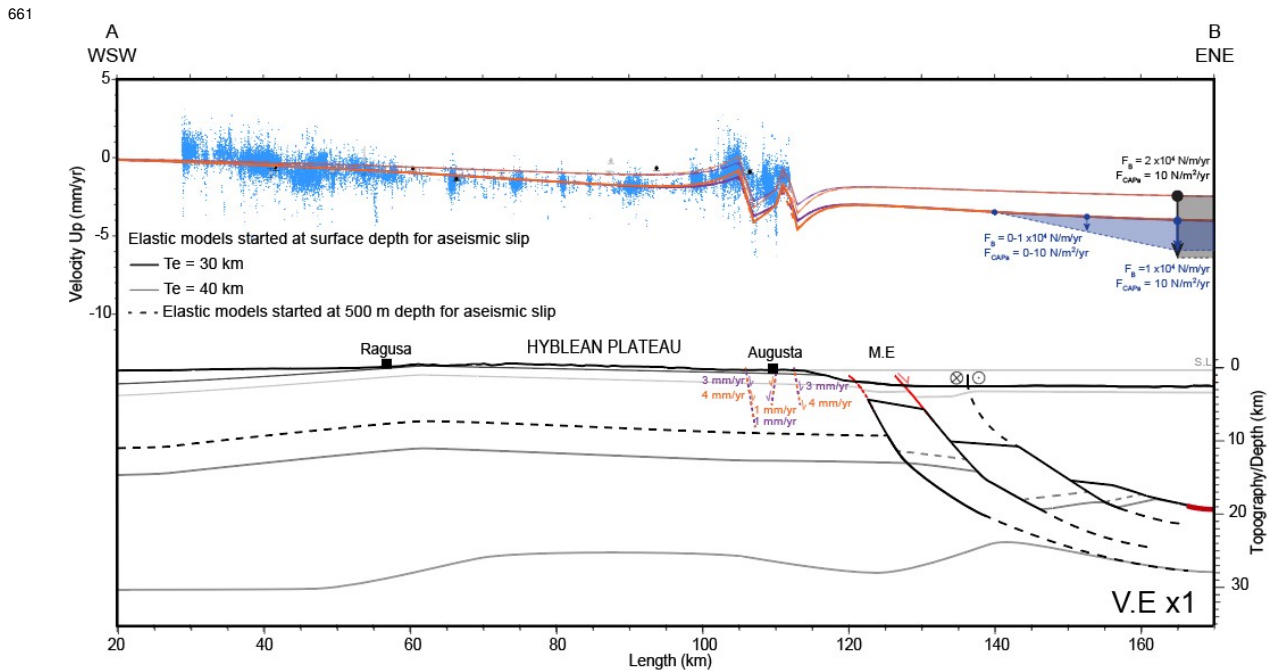


**Figure 10 :** *The final model combining the possible range of the Hyblean continental crust flexural models and the surface deformation (step of 1 km) induced by fault creep (from surface, continuous lines) or active folding in the Augusta-Siracusa coastal domain (from 500 m, dashed lines). In this model, the flexure of the Hyblean continental crust is essentially controlled by the bending force associated with the Ionian slab roll-back ( $F_B$ ) and, to a lesser extent, by the Calabrian accretionary prism load ( $F_{CAPa}$ ). The synthetic structural profile and topography have no vertical exaggeration (V.E.x1).*

662 Interestingly, along the N30°E trending AB synthetic profile, a  $\sim 1^\circ$  generalized  
663 eastward tilting of the HP topography can be evidenced (Figure 4a). The origin of  
664 this tilt, in apparent agreement with the geodetic data, could be rather related to the  
665 Plio-Quaternary formation of the HP (Henriquet et al., 2019). Indeed, geological analyses  
666 suggest that the eastern coast of SE Sicily has been relatively stable over the last million  
667 years, with maximal subsidence and uplift amplitudes of  $\pm 0.2$  mm/yr (Ferranti et al.,  
668 2006). More recently, dating of Late Quaternary marine terraces along the Siracusa-  
669 Augusta coastal domain indicates that the eastern coast of the Hyblean Plateau has  
670 experienced a slow constant uplift during the last 500 Kyr, increasing northward from 0.1  
671 to 0.4 mm/yr (Meschis et al., 2020). On a shorter historical time scale based on Roman  
672 archaeological site studies, Scicchitano et al. (2008), propose that the Siracusa coast has  
673 been slowly uplifting during the last 4 Kyr, albeit with significant uncertainties. These  
674 long-term observations, extending from the Quaternary to historical time, point to a slow  
675 regional uplift, apparently in contradiction with the geodetic data. However, it should be  
676 remembered that we have considered that PS-InSAR measurements primarily document  
677 the interseismic phase. As this stage, the part of the seismic cycle that generates uplift  
678 has not yet been taken into account. Previous calculations (Meschis et al., 2020) shown  
679 that a Mw=7 on the active fault of the Malta Escarpment generate little to no coastal  
680 uplift but early and late post-seismic deformation was not taken into consideration.  
681 In addition, a 500 yr seismic cycle contains other earthquakes contributing to surface  
682 deformation than a single M=7 event. To reconcile long and short-time scale surface  
683 motions, we propose an original seismic cycle model driven by the southward roll-back of  
684 the Ionian subduction (Figure 11).

685

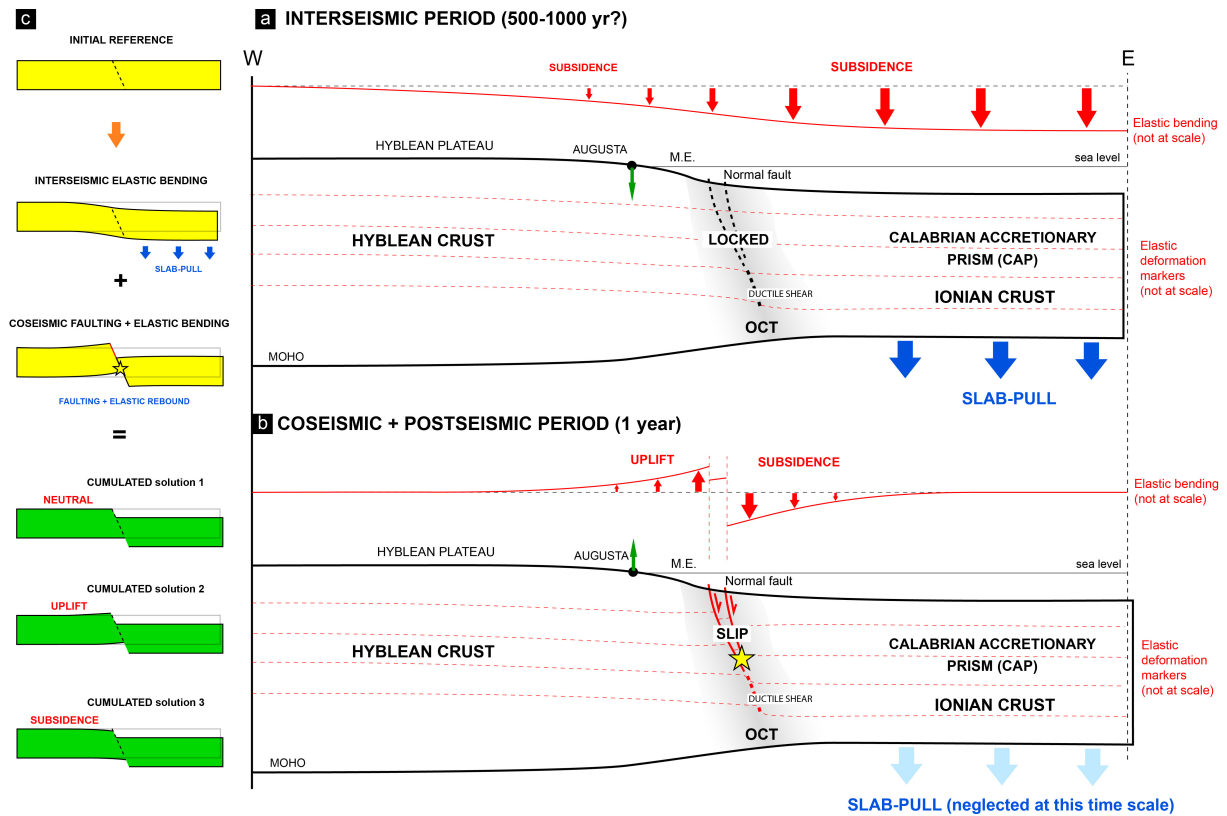


**Figure 11** : Schematic model of seismic cycle for south-eastern Sicily, integrating crustal elastic bending, aseismic, and seismic faulting controlled by slab-pull. a) Interseismic period, b) coseismic and postseismic period, c) different scenarios of the cumulated interseismic, postseismic, and coseismic. This model could reconcile short and long-term observations.

686 During the interseismic phase, the active offshore normal faults affecting the eastern  
 687 HP and Malta Escarpment are locked. The Hyblean and Ionian crusts are coupled and can  
 688 be compared to an elastic beam, bending eastward in response to an increasing downward  
 689 vertical force: the slab pull induced by the Ionian slab roll-back (Figure 11a). Considering  
 690 a minimum 500-yr return period for major earthquakes such as the 1693 Val-di-Noto event  
 691 (Bianca et al., 1999; Meschis et al., 2020) and extrapolating the PS-InSAR measurements  
 692 over this period, coastal subsidence along the Siracusa-Augusta region could reach 1-2 m.  
 693 This subsidence could be dampened to 0.5-1 m if, at the same time, the onshore faults,  
 694 potentially related to extrados deformation, creep aseismically. During the coseismic  
 695 phase, the offshore fault unlocks, and seismic slip induces (for a  $M_w > 7$  earthquake) multi-  
 696 metric subsidence of the hanging wall and an associated decimetric to metric uplift of the  
 697 footwall (e.g., Wells and Coppersmith, 1994) (Figure 11b).

698 The cumulated succession of inter-seismic coastal subsidence and co-seismic uplift  
 699 could result in three scenarios (Figure 11c). If the co-seismic coastal uplift equals the  
 700 cumulated interseismic subsidence, the coastal domain remains stable in the long term.



701 If the former is lower than the latter, as predicted by elastic modeling (Figure 7a), the  
702 coast subsides. Conversely, long-term coastal uplift occurs if coseismic uplift surpasses  
703 interseismic subsidence. Considering that geological data suggest a slow coastal uplift,  
704 this last scenario should be preferred, but additional sources of foot-wall uplift should be  
705 identified (Ferranti et al., 2006; Meschis et al., 2020). At this stage, we can only evoke  
706 raw hypothesis:

- 707 • The buoyancy of the flexed Hyblean crust could significantly increase post-seismic  
708 slip after major earthquakes and thus increase footwall uplift in the coastal region.
- 709 • Further north along the coast, the Ionian slab plunges to great depth and is certainly  
710 detached from the Hyblean continental margin owing to a tear-fault propagation  
711 southward (e.g., Gutscher et al., 2016; Maesano et al., 2020), which could generate  
712 additional stress affecting the surface deformation of the studied region.
- 713 • The inferred interseismic extrado deformation, affecting the coastal domain, could  
714 explain the slow long-term uplift (0.1-0.4 mm/yr) off the eastern coast of the HP  
715 (e.g., Meschis et al., 2020). In that case, extrado deformation activity should be  
716 intermittent, alternating between aseismic fault slip/folding (as presently) and long  
717 periods of quiescence. Such a scenario remains speculative and needs to be mechan-  
718 ically tested.
- 719 • Finally, the potential impact of major subduction earthquake along the Calabrian  
720 Arc on SE Sicily could be also considered (e.g., Gutscher et al., 2016; Carafa et al.,  
721 2018).

## 722 5 Conclusion

723 Present-day deformation of Southeastern Sicily (Hyblean Plateau) reveals specific  
724 long and short-wavelength signals indicating a generalized eastward tilting, reversing a  
725 few kilometers before reaching the eastern coast of the Hyblean Plateau.

726 We propose that the long-wavelength tilt and subsidence can be explained by the  
727 flexure of the Hyblean continental crust in response to the bending force induced by the  
728 southward retreat of the Ionian subduction. Simple flexural modeling, using standard  
729 parameters (elastic thickness of 25-40 km, accretionary prism loading of 5-10 N/m<sup>2</sup>/yr,  
730 and a local increase of bending force of  $1-3 \times 10^4$  N/m/yr or gradually of 0 to  $1-1.5 \times$

731  $10^4$  N/m/yr) support this interpretation.

732 We show that the short wavelength relative coastal uplift, measured geodetically,  
733 could be explained by shallow creep (at 1-4 mm/yr) on ENE steeply dipping normal  
734 faults, related to extrado deformation. Some morphologic evidence of surface deformation,  
735 correlated with leveling data indicating differential surface uplift, seems to corroborate  
736 this hypothesis. However, at this stage, the extrado deformation hypothesis has yet to  
737 be validated. We investigated other hypotheses, such as upwelling mantle flow, volcanic  
738 deflation, and hydrological loading, and found them much less plausible.

739 Finally, we propose an original seismic cycle model in which the surface deformation  
740 of Southeastern Sicily is mainly controlled by bending force induced by the Ionian slab roll-  
741 back, tilting the Hyblean Plateau eastward. The bending of the continental crust causes  
742 aseismic extrados deformation along the eastern coast of the Hyblean Plateau while the  
743 normal faults, affecting the continent-ocean transition, potentially at the origin of the  
744 1693 earthquake, remain currently locked and accumulating interseismic strain. During  
745 a major earthquake, the coastal domain uplifts and compensates for the interseismic  
746 subsidence.

747 To further develop the formulated hypotheses, additional data is required, such  
748 as new high-resolution bathymetric data, onshore and offshore high-resolution seismic  
749 data (CHIRP), and on-site analysis to investigate inferred coastal active faults along  
750 the Augusta-Siracusa region. Besides, acquiring new PS-InSAR data would improve  
751 distinguishing geological processes from human activities. It will be also of interest to  
752 perform more advanced flexural models using 3D finite element modeling techniques.

753

754 **Competing interest:** The first author and co-authors have declared none competing  
755 interests.

756 **Acknowledgments:** This study was funded by the CNRS-INSU-Tellus programs, and  
757 the University of Montpellier (UM). Data supporting materials can be download from the  
758 Easy Data repository (Dataterra ([easydata.earth](http://easydata.earth))). The maps and graphics presented in  
759 this study were generated using the Generic Mapping Tools (GMT) software (Wessel and  
760 Smith, 1998). We are grateful to Serge Lallemand and Nestor Cerpa for helpful discussions  
761 on subduction zone dynamics and flexural modeling.

762 **Author contributions:**



763 Data curation: Amélie Viger, Stéphane Dominguez  
764 Formal analysis: Amélie Viger, Stéphane Dominguez, Michel Peyret, Stéphane Mazzotti,  
765 Maxime Henriquet, Giovanni Barreca, Carmelo Monaco, Adrien Damon  
766 Funding acquisition: Stéphane Dominguez  
767 Ressources: Amélie Viger, Stéphane Dominguez, Maxime Henriquet, Giovanni Barreca,  
768 Carmelo Monaco  
769 Software: Amélie Viger, Adrien Damon, Michel Peyret, Stéphane Mazzotti  
770 Visualization: Amélie Viger, Stéphane Dominguez  
771 Writing – original draft: Amélie Viger, Stéphane Dominguez  
772 Writing – review and editing: Amélie Viger, Stéphane Dominguez, Michel Peyret,  
773 Stéphane Mazzotti, Maxime Henriquet, Giovanni Barreca, Carmelo Monaco, Adrien Da-  
774 mon

## 775 References

- 776 Adam, J., Reuther, C. D., Grasso, M., and Torelli, L.: Active fault kinematics and crustal  
777 stresses along the Ionian margin of southeastern Sicily, *Tectonophysics*, 326, 217–239,  
778 [https://doi.org/10.1016/S0040-1951\(00\)00141-4](https://doi.org/10.1016/S0040-1951(00)00141-4), 2000.
- 779 Afilhado, A., Moulin, M., Aslanian, D., Schnürle, P., Klingelhoefer, F., Nouzé, H., Ra-  
780 bineau, M., Leroux, E., and Beslier, M.-O.: Deep crustal structure across a young  
781 passive margin from wide-angle and reflection seismic data (The SARDINIA Experi-  
782 ment) – II. Sardinia’s margin, *Bulletin de la Société Géologique de France*, 186, 331–351,  
783 <https://doi.org/10.2113/gssgfbull.186.4-5.331>, 2015.
- 784 Almeida, J., Riel, N., Rosas, F. M., Duarte, J. C., and Schellart, W. P.: Polarity-reversal subduction zone initiation triggered by buoyant  
785 plateau obstruction, *Earth and Planetary Science Letters*, 577, 117–195,  
786 <https://www.sciencedirect.com/science/article/pii/S0012821X21004507>,  
787 publisher: Elsevier, 2022.
- 789 Altamimi, Z., Rebischung, P., Métivier, L., and Collilieux, X.: ITRF2014: A new re-  
790 lease of the International Terrestrial Reference Frame modeling nonlinear station mo-  
791 tions, *Journal of Geophysical Research: Solid Earth*, 121, 6109–6131, <https://doi.org/10.1002/2016JB013098>, 2016.
- 793 Anzidei, M., Scicchitano, G., Scardino, G., Bignami, C., Tolomei, C., Vecchio, A., Ser-  
794 pelloni, E., De Santis, V., Monaco, C., Milella, M., Piscitelli, A., and Mastronuzzi, G.:  
795 Relative Sea-Level Rise Scenario for 2100 along the Coast of South Eastern Sicily (Italy)  
796 by InSAR Data, Satellite Images and High-Resolution Topography, *Remote Sensing*,  
797 13, 1108, <https://doi.org/10.3390/rs13061108>, 2021.
- 798 APAT: Carta geologica d’Italia Scala 1: 1 250 000,  
799 <https://www.isprambiente.gov.it/images/progetti/progetto-1250-ita.jpg>,  
800 2005.
- 801 Argnani, A.: Commentary: Deformation Pattern of the Northern Sector of the Malta

- 802 Escarpment (Offshore SE Sicily, Italy): Fault Dimension, Slip Prediction, and Seis-  
803 motectonic Implications, *Frontiers in Earth Science*, 9, 770–364, [https://doi.org/](https://doi.org/10.3389/feart.2021.770364)  
804 10.3389/feart.2021.770364, 2021.
- 805 Argnani, A. and Bonazzi, C.: Malta Escarpment fault zone offshore eastern Sicily:  
806 Pliocene-Quaternary tectonic evolution based on new multichannel seismic data, *Tec-*  
807 *tonics*, 24, <https://doi.org/10.1029/2004TC001656>, 2005.
- 808 Argnani, A., Armigliato, A., Pagnoni, G., Zaniboni, F., Tinti, S., and Bonazzi, C.: Active  
809 tectonics along the submarine slope of south-eastern Sicily and the source of the 11  
810 January 1693 earthquake and tsunamis, *Natural Hazards and Earth System Sciences*,  
811 12, 1311–1319, <https://doi.org/10.5194/nhess-12-1311-2012>, 2012.
- 812 Azzaro, R. and Barbano, M. S.: Analysis of the seismicity of Southeastern Sicily: a pro-  
813 posed tectonic interpretation, <https://www.earth-prints.org/handle/2122/1292>,  
814 2000.
- 815 Behncke, B.: Late Pliocene volcanic island growth and flood basalt-like lava emplacement  
816 in the Hyblean Mountains (SE Sicily): LATE PLIOCENE HYBLEAN VOLCAN-  
817 ISM, *Journal of Geophysical Research: Solid Earth*, 109, n/a–n/a, [https://doi.org/](https://doi.org/10.1029/2003JB002937)  
818 10.1029/2003JB002937, 2004.
- 819 Bianca, M., Monaco, C., Tortorici, L., and Cernobori, L.: Quaternary normal faulting in  
820 southeastern Sicily (Italy): a seismic source for the 1693 large earthquake, *Geophysical*  
821 *Journal International*, 139, 370–394, <https://doi.org/10.1046/j.1365-246x.1999.00942.x>,  
822 1999.
- 823 Bigi, G., Cosentino, D., Parlotto, M., and Sartori, R.: Structural model of Italy, sheet 6,  
824 1991, National Council of Researches Roma, 1991.
- 825 Blewitt, G., Hammond, W., and Kreemer, C.: Harnessing the GPS Data Explosion for  
826 Interdisciplinary Science, *Eos*, 99, <https://doi.org/10.1029/2018eo104623>, 2018.
- 827 Burgmann, R. and Thatcher, W.: Space geodesy: A revolution in crustal deformation  
828 measurements of tectonic processes, *Special Paper of the Geological Society of America*,  
829 500, 397–430, [https://doi.org/10.1130/2013.2500\(12\)](https://doi.org/10.1130/2013.2500(12)), 2013.
- 830 Canova, F., Tolomei, C., Salvi, S., Toscani, G., and Seno, S.: Land subsidence along  
831 the Ionian coast of SE Sicily (Italy), detection and analysis via Small Baseline Subset  
832 (SBAS) multitemporal differential SAR interferometry: LAND SUBSIDENCE ALONG  
833 THE IONIAN COAST OF SE SICILY (ITALY), *Earth Surface Processes and Land-*  
834 *forms*, 37, 273–286, <https://doi.org/10.1002/esp.2238>, 2012.
- 835 Carafa, M. M. C., Kastelic, V., Bird, P., Maesano, F. E., and Valensise, G.: A “Geodetic  
836 Gap” in the Calabrian Arc: Evidence for a Locked Subduction Megathrust?, *Geophys-*  
837 *ical Research Letters*, 45, 1794–1804, <https://doi.org/10.1002/2017GL076554>,  
838 [\\_eprint: https://onlinelibrary.wiley.com/doi/pdf/10.1002/2017GL076554](https://onlinelibrary.wiley.com/doi/pdf/10.1002/2017GL076554), 2018.
- 839 Carminati, E. and Doglioni, C.: Mediterranean Tectonics, in: *Encyclopedia of Geology*,  
840 pp. 135–146, <https://doi.org/10.1016/B0-12-369396-9/00135-0>, 2005.
- 841 Carminati, E., Lustrino, M., and Doglioni, C.: Geodynamic evolution of the central and  
842 western Mediterranean: Tectonics vs. igneous petrology constraints, *Tectonophysics*,  
843 579, 173–192, <https://doi.org/10.1016/j.tecto.2012.01.026>, 2012.
- 844 Catalano, R., Doglioni, C., and Merlini, S.: On the Mesozoic Ionian Basin, *Geophysical*  
845 *Journal International*, 144, 49–64, <https://doi.org/10.1046/j.0956-540X.2000.01287.x>,  
846 2001.

- 847 Chen, Y.-G., Lai, K.-Y., Lee, Y.-H., Suppe, J., Chen, W.-S., Lin, Y.-N. N., Wang, Y.,  
848 Hung, J.-H., and Kuo, Y.-T.: Coseismic fold scarps and their kinematic behavior in the  
849 1999 Chi-Chi earthquake Taiwan, *Journal of Geophysical Research: Solid Earth*, 112,  
850 <https://doi.org/10.1029/2006JB004388>, 2007.
- 851 Civello, S. and Margheriti, L.: Toroidal mantle flow around the Calabrian slab (Italy) from  
852 SKS splitting: TOROIDAL FLOW AROUND THE CALABRIAN SLAB, *Geophysical*  
853 *Research Letters*, 31, n/a–n/a, <https://doi.org/10.1029/2004GL019607>, 2004.
- 854 Cloetingh, S., Ziegler, P., Beekman, F., Burov, E., Garcia-Castellanos, D., and Matenco,  
855 L.: Tectonic Models for the Evolution of Sedimentary Basins, in: *Treatise on Geo-*  
856 *physics*, pp. 513–592, Elsevier, ISBN 978-0-444-53803-1, [https://doi.org/10.1016/B978-](https://doi.org/10.1016/B978-0-444-53802-4.00117-2)  
857 [0-444-53802-4.00117-2](https://doi.org/10.1016/B978-0-444-53802-4.00117-2), 2015.
- 858 Cultrera, F., Barreca, G., Scarfi, L., and Monaco, C.: Fault reactivation by  
859 stress pattern reorganization in the Hyblean foreland domain of SE Sicily (Italy)  
860 and seismotectonic implications, *Tectonophysics*, 661, 215–228, [https://doi.org/](https://doi.org/10.1016/j.tecto.2015.08.043)  
861 [10.1016/j.tecto.2015.08.043](https://doi.org/10.1016/j.tecto.2015.08.043), 2015.
- 862 D’Agostino, N., D’Anastasio, E., Gervasi, A., Guerra, I., Nedimović, M. R., See-  
863 ber, L., and Steckler, M.: Forearc extension and slow rollback of the Calabrian  
864 Arc from GPS measurements, *Geophysical Research Letters*, 38, [https://doi.org/](https://doi.org/10.1029/2011GL048270)  
865 [10.1029/2011GL048270](https://doi.org/10.1029/2011GL048270), 2011.
- 866 D’Agostino, N., Silverii, F., Amoroso, O., Convertito, V., Fiorillo, F., Ventafriidda, G., and  
867 Zollo, A.: Crustal Deformation and Seismicity Modulated by Groundwater Recharge  
868 of Karst Aquifers, *Geophysical Research Letters*, 45, 12,253–12,262, [https://doi.org/](https://doi.org/10.1029/2018GL079794)  
869 [10.1029/2018GL079794](https://doi.org/10.1029/2018GL079794), 2018.
- 870 Dellong, D., Klingelhoefer, F., Kopp, H., Graindorge, D., Margheriti, L., Moretti, M.,  
871 Murphy, S., and Gutscher, M.-A.: Crustal Structure of the Ionian Basin and Eastern  
872 Sicily Margin: Results From a Wide-Angle Seismic Survey, *Journal of Geophysical*  
873 *Research: Solid Earth*, 123, 2090–2114, <https://doi.org/10.1002/2017JB015312>, 2018.
- 874 Dellong, D., Klingelhoefer, F., Dannowski, A., Kopp, H., Murphy, S., Graindorge, D.,  
875 Margheriti, L., Moretti, M., Barreca, G., Scarfi, L., Polonia, A., and Gutscher, M.-A.:  
876 Geometry of the Deep Calabrian Subduction (Central Mediterranean Sea) From Wide-  
877 Angle Seismic Data and 3-D Gravity Modeling, *Geochemistry, Geophysics, Geosystems*,  
878 21, 2019GC008 586, <https://doi.org/10.1029/2019GC008586>, 2020.
- 879 Faccenna, C., Becker, T. W., Lucente, F. P., Jolivet, L., and Rossetti, F.: History of  
880 subduction and back-arc extension in the Central Mediterranean, *Geophysical Journal*  
881 *International*, 145, 809–820, <https://doi.org/10.1046/j.0956-540x.2001.01435.x>, 2001.
- 882 Faccenna, C., Civetta, L., D’Antonio, M., Funiciello, F., Margheriti, L., and Piro-  
883 mallo, C.: Constraints on mantle circulation around the deforming Calabrian slab,  
884 *Geophysical Research Letters*, 32, <https://doi.org/10.1029/2004GL021874>,  
885 [\\_eprint:  
https://onlinelibrary.wiley.com/doi/pdf/10.1029/2004GL021874](https://onlinelibrary.wiley.com/doi/pdf/10.1029/2004GL021874), 2005.
- 886 Faccenna, C., Molin, P., Orecchio, B., Olivetti, V., Bellier, O., Funiciello, F., Minelli,  
887 L., Piromallo, C., and Billi, A.: Topography of the Calabria subduction zone (southern  
888 Italy): Clues for the origin of Mt. Etna, *Tectonics*, 30, 2010TC002 694, [https://doi.org/](https://doi.org/10.1029/2010TC002694)  
889 [10.1029/2010TC002694](https://doi.org/10.1029/2010TC002694), 2011.
- 890 Ferranti, L., Antonioli, F., Mauz, B., Amorosi, A., Dai Pra, G., Mastronuzzi, G.,  
891 Monaco, C., Orrù, P., Pappalardo, M., Radtke, U., Renda, P., Romano, P., Sansò,  
892 P., and Verrubbi, V.: Markers of the last interglacial sea-level high stand along

- 893 the coast of Italy: Tectonic implications, *Quaternary International*, 145-146, 30–54,  
894 <https://doi.org/10.1016/j.quaint.2005.07.009>, 2006.
- 895 Ferranti, L., Antonioli, F., Anzidei, M., Monaco, C., and Stocchi, P.: The timescale  
896 and spatial extent of recent vertical tectonic motions in Italy: insights from rela-  
897 tive sea-level changes studies, *Journal of the Virtual Explorer*, 36, [https://doi.org/](https://doi.org/10.3809/jvirtex.2010.00255)  
898 [10.3809/jvirtex.2010.00255](https://doi.org/10.3809/jvirtex.2010.00255), 2010.
- 899 Finetti, I. R., Lentini, F., Carbone, S., Del Ben, A., Di Stefano, A., Forlin, E., Guarnieri,  
900 P., Pipan, M., and Prizzon, A.: Geological outline of Sicily and lithospheric tectono-  
901 dynamics of its Tyrrhenian margin from new CROP seismic data, *CROP Project: deep*  
902 *seismic exploration of the central Mediterranean and Italy*, pp. 319–375, 2005.
- 903 Frizon De Lamotte, D., Raulin, C., Mouchot, N., Wrobel-Daveau, J.-C., Blanpied, C., and  
904 Ringenbach, J.-C.: The southernmost margin of the Tethys realm during the Mesozoic  
905 and Cenozoic: Initial geometry and timing of the inversion processes, *Tectonics*, 30,  
906 2010TC002691, <https://doi.org/10.1029/2010TC002691>, 2011.
- 907 Funicello, R., Parotto, M., Praturlon, A., and Bigi, G.: Carta tettonica d'Italia alla scala  
908 1: 1.500. 000, *CNR Progetto Finalizzato Geodinamica, Pubbl*, 269, 1981.
- 909 Gallen, S. F., Seymour, N. M., Glotzbach, C., Stockli, D. F., and O'Sullivan, P.: Calabrian  
910 forearc uplift paced by slab–mantle interactions during subduction retreat, *Nature Geo-*  
911 *science*, pp. 1–8, 2023.
- 912 Gambino, S., Barreca, G., Gross, F., Monaco, C., Krastel, S., and Gutscher, M.-A.: De-  
913 formation Pattern of the Northern Sector of the Malta Escarpment (Offshore SE Sicily,  
914 Italy): Fault Dimension, Slip Prediction, and Seismotectonic Implications, *Frontiers in*  
915 *Earth Science*, 8, 594176, <https://doi.org/10.3389/feart.2020.594176>, 2021.
- 916 Gambino, S., Barreca, G., Bruno, V., De Guidi, G., Ferlito, C., Gross, F., Mat-  
917 tia, M., Scarfi, L., and Monaco, C.: Transtension at the Northern Termination  
918 of the Alfeo-Etna Fault System (Western Ionian Sea, Italy): Seismotec-  
919 tonic Implications and Relation with Mt. Etna Volcanism, *Geosciences*, 12, 128,  
920 <https://www.mdpi.com/2076-3263/12/3/128>, publisher: MDPI, 2022a.
- 921 Gambino, S., Barreca, G., Gross, F., Monaco, C., Gutscher, M.-A., and Alsop, G. I.:  
922 Assessing the rate of crustal extension by 2D sequential restoration analysis: A case  
923 study from the active portion of the Malta Escarpment, *Basin Research*, 34, 321–341,  
924 <https://doi.org/10.1111/bre.12621>, 2022b.
- 925 Goes, S., Giardini, D., Jenny, S., Hollenstein, C., Kahle, H. G., and Geiger, A.: A  
926 recent tectonic reorganization in the south-central Mediterranean, *Earth and Planetary*  
927 *Science Letters*, 226, 335–345, <https://doi.org/10.1016/j.epsl.2004.07.038>, 2004.
- 928 Grasso, M. t. and Lentini, F.: Sedimentary and tectonic evolution of the eastern Hyblean  
929 Plateau (southeastern Sicily) during late Cretaceous to Quaternary time, *Palaeogeog-*  
930 *raphy, Palaeoclimatology, Palaeoecology*, 39, 261–280, 1982.
- 931 Grillo, B., Braitenberg, C., Devoti, R., and Nagy, I.: The study of karstic aquifers by  
932 geodetic measurements in Bus de la Genziana station – Cansiglio plateau (Northeastern  
933 Italy), *Acta Carsologica*, 40, <https://doi.org/10.3986/ac.v40i1.35>, 2011.
- 934 Gueguen, E., Doglioni, C., and Fernandez, M.: On the post-25 Ma geodynamic evo-  
935 lution of the western Mediterranean, *Tectonophysics*, 298, 259–269, [https://doi.org/](https://doi.org/10.1016/S0040-1951(98)00189-9)  
936 [10.1016/S0040-1951\(98\)00189-9](https://doi.org/10.1016/S0040-1951(98)00189-9), 1998.
- 937 Gutscher, M.-A., Roger, J., Baptista, M.-A., Miranda, J. M., and Tinti, S.: Source  
938 of the 1693 Catania earthquake and tsunami (southern Italy): New evidence from

- 939 tsunami modeling of a locked subduction fault plane, *Geophysical Research Letters*,  
940 33, <https://doi.org/10.1029/2005GL025442>, 2006.
- 941 Gutscher, M.-A., Dominguez, S., de Lepinay, B. M., Pinheiro, L., Gallais, F., Babonneau,  
942 N., Cattaneo, A., Le Faou, Y., Barreca, G., Micallef, A., and Rovere, M.: Tectonic  
943 expression of an active slab tear from high-resolution seismic and bathymetric data off-  
944 shore Sicily (Ionian Sea), *Tectonics*, 35, 39–54, <https://doi.org/10.1002/2015TC003898>,  
945 2016.
- 946 Handy, M. R., M. Schmid, S., Bousquet, R., Kissling, E., and Bernoulli, D.: Recon-  
947 ciling plate-tectonic reconstructions of Alpine Tethys with the geological–geophysical  
948 record of spreading and subduction in the Alps, *Earth-Science Reviews*, 102, 121–158,  
949 <https://doi.org/10.1016/j.earscirev.2010.06.002>, 2010.
- 950 Handy, M. R., Ustaszewski, K., and Kissling, E.: Reconstructing the  
951 Alps–Carpathians–Dinarides as a key to understanding switches in subduction  
952 polarity, slab gaps and surface motion, *International Journal of Earth Sciences*, 104,  
953 1–26, <https://doi.org/10.1007/s00531-014-1060-3>, 2015.
- 954 Hayes, G. P., Moore, G. L., Portner, D. E., Hearne, M., Flamme, H., Furtney, M., and  
955 Smoczyk, G. M.: Slab2, a comprehensive subduction zone geometry model, *Science*,  
956 362, 58–61, <https://doi.org/10.1126/science.aat4723>, 2018.
- 957 Henriquet, M., Dominguez, S., Barreca, G., Malavieille, J., Cadio, C., and  
958 Monaco, C.: Deep Origin of the Dome-Shaped Hyblean Plateau, Southeastern  
959 Sicily: A New Tectono-Magmatic Model, *Tectonics*, 38, 4488–4515, <https://doi.org/10.1029/2019TC005548>, 2019.
- 961 Henriquet, M., Dominguez, S., Barreca, G., Malavieille, J., and Monaco, C.: Struc-  
962 tural and tectono-stratigraphic review of the Sicilian orogen and new insights  
963 from analogue modeling, *Earth-Science Reviews*, 208, 103 257, <https://doi.org/10.1016/j.earscirev.2020.103257>, 2020.
- 965 Henriquet, M., Peyret, M., Dominguez, S., Barreca, G., Monaco, C., and Mazzotti, S.:  
966 Present-Day Surface Deformation of Sicily Derived From Sentinel-1 InSAR Time-Series,  
967 *Journal of Geophysical Research: Solid Earth*, 127, e2021JB023 071, <https://doi.org/10.1029/2021JB023071>, 2022.
- 969 Istituto Nazionale di Geofisica e Vulcanologia (INGV): Rete Sismica Nazionale (RSN),  
970 pp. approx. 27 GB per day of new waveform data, approx. 415 active seismic sta-  
971 tions, the archive totals to more than 600 distinct seismic stations, <https://doi.org/10.13127/SD/X0FXNH7QFY>, 2005.
- 973 Jolivet, L.: Tethys and Apulia (Adria), 100 years of reconstructions, *Comptes Rendus.*  
974 *Géoscience*, 355, 9–28, <https://doi.org/10.5802/crgeos.198>, 2023.
- 975 Klingelhoefer, F., Déverchère, J., Graindorge, D., Aïdi, C., Badji, R., Bouyahiaoui, B.,  
976 Leprêtre, A., Mihoubi, A., Beslier, M.-O., Charvis, P., Schnurle, P., Sage, F., Medaouri,  
977 M., Arab, M., Bracene, R., Yelles-Chaouche, A., Badsì, M., Galvé, A., and Géli, L.: For-  
978 mation, segmentation and deep crustal structure variations along the Algerian margin  
979 from the SPIRAL seismic experiment, *Journal of African Earth Sciences*, 186, 104433,  
980 <https://doi.org/10.1016/j.jafrearsci.2021.104433>, 2022.
- 981 Kreemer, C., Blewitt, G., and Klein, E. C.: A geodetic plate motion and Global Strain  
982 Rate Model, *Geochemistry, Geophysics, Geosystems*, 15, 3849–3889, <https://doi.org/10.1002/2014GC005407>, 2014.
- 984 Lallemand, S., Heuret, A., Faccenna, C., and Funiciello, F.: Subduction dynamics as

- 985 revealed by trench migration: SUBDUCTION DYNAMICS, *Tectonics*, 27, n/a–n/a,  
986 <https://doi.org/10.1029/2007TC002212>, 2008.
- 987 Lentini, F. and Carbone, S.: Geologia della Sicilia-geology of Sicily, *Memorie Descr. Carta*  
988 *Geologica d'Italia*, 95, 7–414, 2014.
- 989 Levandowski, W., Herrmann, R. B., Briggs, R., Boyd, O., and Gold, R.: An updated  
990 stress map of the continental United States reveals heterogeneous intraplate stress,  
991 *Nature Geoscience*, 11, 433–437, <https://doi.org/10.1038/s41561-018-0120-x>, 2018.
- 992 Li, T., Chen, J., Thompson, J. A., Burbank, D. W., and Yang, H.: Hinge-migrated  
993 fold-scarp model based on an analysis of bed geometry: A study from the Mingyao  
994 anticline, southern foreland of Chinese Tian Shan, *Journal of Geophysical Research:*  
995 *Solid Earth*, 120, 6592–6613, <https://doi.org/10.1002/2015JB012102>, 2015.
- 996 Lipparini, L., Chiacchieri, D., Bencini, R., and Micallef, A.: Extensive freshened ground-  
997 water resources emplaced during the Messinian sea-level drawdown in southern Sicily,  
998 Italy, *Communications Earth & Environment*, 4, 430, <https://doi.org/10.1038/s43247-023-01077-w>, 2023.
- 1000 Maesano, F. E., Tiberti, M. M., and Basili, R.: The Calabrian Arc: three-dimensional  
1001 modelling of the subduction interface, *Scientific Reports*, 7, 8887, <https://doi.org/10.1038/s41598-017-09074-8>, 2017.
- 1003 Maesano, F. E., Tiberti, M. M., and Basili, R.: Deformation and fault propagation at the  
1004 lateral termination of a subduction zone: the Alfeo Fault System in the Calabrian Arc,  
1005 southern Italy, *Frontiers in Earth Science*, 8, 107, 2020.
- 1006 Masson, C., Mazzotti, S., and Vernant, P.: Precision of continuous GPS velocities from  
1007 statistical analysis of synthetic time series, *Solid Earth*, 10, 329–342, <https://doi.org/10.5194/se-10-329-2019>, 2019.
- 1009 Mastrolembo, B., Serpelloni, E., Argnani, A., Bonforte, A., Burgmann, R., Anzidei,  
1010 M., Baldi, P., and Puglisi, G.: Fast geodetic strain-rates in eastern Sicily (south-  
1011 ern Italy): New insights into block tectonics and seismic potential in the area of  
1012 the great 1693 earthquake, *Earth and Planetary Science Letters*, 404, <https://doi.org/10.1016/j.epsl.2014.07.025>, 2014.
- 1014 Mattia, M., Bruno, V., Cannavò, F., and Palano, M.: Evidences of a contractional pattern  
1015 along the northern rim of the Hyblean Plateau (Sicily, Italy) from GPS data, *Geologica*  
1016 *Acta: an international earth science journal*, 10, 1–8, 2012.
- 1017 Mazzotti, S., James, T. S., Henton, J., and Adams, J.: GPS crustal strain, postglacial  
1018 rebound, and seismic hazard in eastern North America: The Saint Lawrence valley ex-  
1019 ample: CRUSTAL STRAIN IN SAINT LAWRENCE VALLEY, *Journal of Geophysical*  
1020 *Research: Solid Earth*, 110, <https://doi.org/10.1029/2004JB003590>, 2005.
- 1021 Meschis, M., Scicchitano, G., Roberts, G. P., Robertson, J., Barreca, G., Monaco, C.,  
1022 Spampinato, C., Sahy, D., Antonioli, F., Mildon, Z. K., and Scardino, G.: Regional De-  
1023 formation and Offshore Crustal Local Faulting as Combined Processes to Explain Uplift  
1024 Through Time Constrained by Investigating Differentially Uplifted Late Quaternary Pa-  
1025 leoshorelines: The Foreland Hyblean Plateau, SE Sicily, *Tectonics*, 39, e2020TC006187,  
1026 <https://doi.org/10.1029/2020TC006187>, 2020.
- 1027 Michael, A. J.: Determination of stress from slip data: Faults and folds, *Journal of Geo-*  
1028 *physical Research: Solid Earth*, 89, <https://doi.org/10.1029/JB089iB13p11517>, 1984.
- 1029 Milano, M., Kelemework, Y., La Manna, M., Fedi, M., Montanari, D., and Iorio, M.:

- 1030 Crustal structure of Sicily from modelling of gravity and magnetic anomalies, *Scientific*  
1031 *Reports*, 10, 16 019, 2020.
- 1032 Minelli, L. and Faccenna, C.: Evolution of the Calabrian accretionary wedge (central  
1033 Mediterranean): CALABRIAN ACCRETIONARY WEDGE, *Tectonics*, 29, n/a–n/a,  
1034 <https://doi.org/10.1029/2009TC002562>, 2010.
- 1035 Mogi, K.: Relations between the eruptions of various volcanoes and the deformations of  
1036 the ground surfaces around them, *Earthquake Research Institute*, 36, 99–134, 1958.
- 1037 Monaco, C. and Tortorici, L.: Active faulting in the Calabrian  
1038 arc and eastern Sicily, *Journal of Geodynamics*, 29, 407–424,  
1039 <https://www.sciencedirect.com/science/article/pii/S0264370799000526>,  
1040 2000.
- 1041 Palano, M., Ferranti, L., Monaco, C., Mattia, M., Aloisi, M., Bruno, V., Cannavò,  
1042 F., and Siligato, G.: GPS velocity and strain fields in Sicily and southern Cal-  
1043 abria, Italy: Updated geodetic constraints on tectonic block interaction in the central  
1044 Mediterranean, *Journal of Geophysical Research: Solid Earth*, 117, <https://doi.org/10.1029/2012JB009254>, 2012.
- 1046 Prada, M., Sallarès, V., Ranero, C. R., Vendrell, M. G., Grevemeyer, I., Zitellini, N.,  
1047 and de Franco, R.: A cross-section of crustal domains and tectonic structure across the  
1048 Central Tyrrhenian Basin: from back-arc extension to mantle exhumation, in: *EGU*  
1049 *General Assembly Conference Abstracts*, p. 9844, 2014.
- 1050 Rosenbaum, G., Lister, G. S., and Duboz, C.: Reconstruction of the tectonic evolution of  
1051 the western Mediterranean since the Oligocene, *Journal of the Virtual Explorer*, 2002.
- 1052 Rovida, A., Locati, M., Camassi, R., Lolli, B., Gasperini, P., and Antonucci, A.:  
1053 *Catálogo Paramétrico dei Terremoti Italiani (CPTI15)*, versione 4.0, <https://doi.org/10.13127/CPTI/CPTI15.4>, 2022.
- 1055 Sapin, F., Ringenbach, J.-C., and Clerc, C.: Rifted margins classification and forcing  
1056 parameters, *Scientific Reports*, 11, 8199, <https://doi.org/10.1038/s41598-021-87648-3>,  
1057 2021.
- 1058 Scandone, P., Patacca, E., Radoicic, R., Ryan, W. B. F., Cita, M. B., Rawson, M., Chezar,  
1059 H., Miller, E., McKenzie, J., and Rossi, S.: Mesozoic and Cenozoic rocks from Malta  
1060 escarpment (central Mediterranean), *AAPG Bulletin*, 65, 1299–1319, 1981.
- 1061 Scarfi, L., Barberi, G., Barreca, G., Cannavò, F., Koulakov, I., and Patanè, D.: Slab  
1062 narrowing in the Central Mediterranean: the Calabro-Ionian subduction zone as imaged  
1063 by high resolution seismic tomography, *Scientific Reports*, 8, 5178, <https://doi.org/10.1038/s41598-018-23543-8>, 2018.
- 1065 Schmincke, H.-U., Behncke, B., Grasso, M., and Raffi, S.: Evolution of the northwestern  
1066 Iblean Mountains, Sicily: uplift, Pliocene/Pleistocene sea-level changes, paleoenviron-  
1067 ment, and volcanism, *Geologische Rundschau*, 86, 637–669, 1997.
- 1068 Scicchitano, G., Antonioli, F., Berlinghieri, E. F. C., Dutton, A., and Monaco, C.: Sub-  
1069 merged archaeological sites along the Ionian coast of southeastern Sicily (Italy) and  
1070 implications for the Holocene relative sea-level change, *Quaternary Research*, 70, 26–  
1071 39, <https://doi.org/10.1016/j.yqres.2008.03.008>, 2008.
- 1072 Scicchitano, G., Gambino, S., Scardino, G., Barreca, G., Gross, F., Mastronuzzi, G., and  
1073 Monaco, C.: The enigmatic 1693 AD tsunamis in the eastern Mediterranean Sea: new  
1074 insights on the triggering mechanisms and propagation dynamics, *Scientific Reports*,  
1075 12, 9573, <https://doi.org/10.1038/s41598-022-13538-x>, 2022.

- 1076 Scognamiglio, L., Tinti, E., and Quintiliani, M.: Time Domain Moment Tensor (TDMT),  
1077 <https://doi.org/10.13127/TDMT>, 2006.
- 1078 SgROI, T., de Nardis, R., and Lavecchia, G.: Crustal structure and seis-  
1079 motectonics of central Sicily (southern Italy): new constraints from in-  
1080 strumental seismicity, *Geophysical Journal International*, 189, 1237–1252,  
1081 <https://academic.oup.com/gji/article-abstract/189/3/1237/608535>, 2012.
- 1082 Silverii, F., D’Agostino, N., Métois, M., Fiorillo, F., and Ventafridda, G.: Transient  
1083 deformation of karst aquifers due to seasonal and multiyear groundwater variations  
1084 observed by GPS in southern Apennines (Italy), *Journal of Geophysical Research: Solid  
1085 Earth*, 121, 8315–8337, <https://doi.org/10.1002/2016JB013361>, 2016.
- 1086 S.I.T.R. regione Siciliana: Scheda metadato DATASET Mod-  
1087 ello digitale del terreno (MDT) 2m - Volo ATA 2012 2013  
1088 - Regione Siciliana - S.I.T.R. Infrastruttura Dati Territoriali,  
1089 <https://www.sitr.regione.sicilia.it/geoportale/it/metadata/details/946>,  
1090 2013.
- 1091 Spampinato, C. R., Braitenberg, C., Monaco, C., and Scicchitano, G.: Analysis of verti-  
1092 cal movements in eastern Sicily and southern Calabria (Italy) through geodetic level-  
1093 ing data, *Journal of Geodynamics*, 66, 1–12, <https://doi.org/10.1016/j.jog.2012.12.002>,  
1094 2013.
- 1095 Speranza, F., Minelli, L., Pignatelli, A., and Chiappini, M.: The Ionian Sea: The oldest  
1096 in situ ocean fragment of the world?: MAGNETIC MODELLING OF THE IONIAN  
1097 SEA, *Journal of Geophysical Research: Solid Earth*, 117, n/a–n/a, <https://doi.org/10.1029/2012JB009475>, 2012.
- 1099 Stampfli, G., Borel, G., Marchant, R., and Mosar, J.: Western Alps geological con-  
1100 straints on western Tethyan reconstructions, *Journal of the Virtual Explorer*, 08,  
1101 <https://doi.org/10.3809/jvirtex.2002.00057>, 2002.
- 1102 Stephenson, O. L., Liu, Y.-K., Yunjun, Z., Simons, M., Rosen, P., and Xu, X.: The Im-  
1103 pact of Plate Motions on Long-Wavelength InSAR-Derived Velocity Fields, *Geophysical  
1104 Research Letters*, 49, e2022GL099835, <https://doi.org/10.1029/2022GL099835>, 2022.
- 1105 TesauRO, M., Audet, P., Kaban, M. K., Bürgmann, R., and Cloetingh, S.: The effective  
1106 elastic thickness of the continental lithosphere: Comparison between rheological and  
1107 inverse approaches: *Te OF THE CONTINENTAL LITHOSPHERE*, *Geochemistry,  
1108 Geophysics, Geosystems*, 13, <https://doi.org/10.1029/2012GC004162>, 2012.
- 1109 Toda, S., Stein, R. S., Sevilgen, V., and Lin, J.: Coulomb 3.3 Graphic-rich deformation  
1110 and stress-change software for earthquake, tectonic, and volcano research and teach-  
1111 ing—user guide, US Geological Survey open-file report, 1060, 63, 2011.
- 1112 Trua, T., Serri, G., and Marani, M. P.: Lateral flow of African mantle below the nearby  
1113 Tyrrhenian plate: geochemical evidence, *Terra Nova*, 15, 433–440, <https://doi.org/10.1046/j.1365-3121.2003.00509.x>, 2003.
- 1115 Tugend, J., Chamot-Rooke, N., Arsenikos, S., Blanpied, C., and Frizon De Lamotte,  
1116 D.: Geology of the Ionian Basin and Margins: A Key to the East Mediterranean  
1117 Geodynamics, *Tectonics*, 38, 2668–2702, <https://doi.org/10.1029/2018TC005472>, 2019.
- 1118 Turcotte, D. L. and Schubert, G.: *Geodynamics*, Cambridge University Press, Cambridge,  
1119 United Kingdom, third edition edn., ISBN 978-1-107-00653-9 978-0-521-18623-0, 2014.
- 1120 Van Hinsbergen, D. J., Torsvik, T. H., Schmid, S. M., Maçenco, L. C., Maffione, M.,  
1121 Vissers, R. L., Gürer, D., and Spakman, W.: Orogenic architecture of the Mediter-



- 1122 ranean region and kinematic reconstruction of its tectonic evolution since the Triassic,  
1123 Gondwana Research, 81, 79–229, <https://doi.org/10.1016/j.gr.2019.07.009>, 2020.
- 1124 Vavryčuk, V.: Iterative joint inversion for stress and fault orientations from fo-  
1125 cal mechanisms, *Geophysical Journal International*, 199, 69–77, <https://doi.org/10.1093/gji/ggu224>, 2014.
- 1127 ViDEPI: Progetto ViDEPI-Visibilità dei Dati Afferenti All’Attività di Esplorazione Petro-  
1128 lifera in Italia. 2016 (Last Upgrade).
- 1129 Vilardo, G., Ventura, G., Terranova, C., Matano, F., and Nardò, S.: Ground deformation  
1130 due to tectonic, hydrothermal, gravity, hydrogeological, and anthropic processes in  
1131 the Campania Region (Southern Italy) from Permanent Scatterers Synthetic Aperture  
1132 Radar Interferometry, *Remote Sensing of Environment*, 113, 197–212, <https://doi.org/10.1016/j.rse.2008.09.007>, 2009.
- 1134 Vollrath, A., Zucca, F., Bekaert, D., Bonforte, A., Guglielmino, F., Hooper, A., and  
1135 Stramondo, S.: Decomposing DInSAR Time-Series into 3-D in Combination with GPS  
1136 in the Case of Low Strain Rates: An Application to the Hyblean Plateau, Sicily, Italy,  
1137 *Remote Sensing*, 9, 33, <https://doi.org/10.3390/rs9010033>, 2017.
- 1138 Watts, A. B. and Zhong, S.: Observations of  $\bar{\epsilon}$ -exure and the rheology of oceanic litho-  
1139 sphere, 2000.
- 1140 Wells, D. L. and Coppersmith, K. J.: New empirical relationships among  
1141 magnitude, rupture length, rupture width, rupture area, and surface dis-  
1142 placement, *Bulletin of the seismological Society of America*, 84, 974–1002,  
1143 <https://pubs.geoscienceworld.org/ssa/bssa/article-abstract/84/4/974/119792>,  
1144 1994.
- 1145 Wessel, P. and Smith, W. H. F.: New, improved version of generic mapping tools re-  
1146 leased, *Eos, Transactions American Geophysical Union*, 79, 579–579, <https://doi.org/10.1029/98EO00426>, 1998.
- 1148 White, A. M., Gardner, W. P., Borsa, A. A., Argus, D. F., and Martens,  
1149 H. R.: A Review of GNSS/GPS in Hydrogeodesy: Hydrologic Loading Appli-  
1150 cations and Their Implications for Water Resource Research, *Water Resources*  
1151 *Research*, 58, e2022WR032078, <https://doi.org/10.1029/2022WR032078>,  
1152 [\\_eprint:  
https://onlinelibrary.wiley.com/doi/pdf/10.1029/2022WR032078](https://onlinelibrary.wiley.com/doi/pdf/10.1029/2022WR032078), 2022.
- 1153 Wickert, A. D.: Open-source modular solutions for flexural isostasy: gFlex v1.0, *Geo-*  
1154 *scientific Model Development*, 9, 997–1017, <https://doi.org/10.5194/gmd-9-997-2016>,  
1155 2016.
- 1156 Wortel, M. J. R. and Spakman, W.: Subduction and Slab Detachment in  
1157 the Mediterranean-Carpathian Region, *Science*, 290, 1910–1917, <https://doi.org/10.1126/science.290.5498.1910>, 2000.
- 1159 Zitellini, N., Ranero, C. R., Loreto, M. F., Ligi, M., Pastore, M., D’Oriano, F., Sallares,  
1160 V., Grevemeyer, I., Moeller, S., and Prada, M.: Recent inversion of the Tyrrhenian  
1161 Basin, *Geology*, 48, 123–127, <https://doi.org/10.1130/G46774.1>, 2020.